Meteorol. Atmos. Phys. 53, 185–222 (1994)

Meteorology and Atmospheric Physics

551.551.8

[1] Bureau of Meteorology Research Centre, Melbourne, Australia
[2] U.S.R.A., NASA Goddard Space Flight Center, Greenbelt, Maryland, U.S.A.
[3] NASA Goddard Space Flight Center Greenbelt, Maryland, U.S.A.

Development and Structure of a Maritime Continent Thunderstorm

T. D. Keenan[1], B. Ferrier[2], and J. Simpson[3]

With 17 Figures

Received June 18, 1993
Revised September 30, 1993

Summary

The evaluation of a maritime continent thunderstorm complex (Hector) occurring over Bathurst and Melville Islands north of Darwin, Australia (12° S, 131° E) is investigated primarily using Doppler radar data. Thunderstorm formation follows the development of sea breeze circulations and a period of shallow non-precipitating convection. Evidence exists for initiation of long-lived and organised convection on the sea breeze fronts, although short-lived, scattered convection is apparent earlier in the day. Merging of the convective systems is observed in regions of enhanced low-level convergence related to sea breeze circulations. The merged convective complex is initially aligned in an almost east-west direction consistent with the low-level forcing. The merged complex results in rapid vertical development with updraughts reaching 40 m s^{-1} and echo tops reaching 20 km height. Maximum precipitation production occurs during this merger phase. On the perimeter of the merged convective complex, evidence exists for front-to-rear updraughts sloped over lower-level downdraughts with rear-to-front relative flow and forward propagating cold pools. The mature phase is dominated by this convection and the complex re-orientates in the prevailing easterly vertical shear to an approximate north-south direction, then moves westward off the islands with the classic multicellular squall-like structure.

The one-dimensional cloud model of Ferrier and Houze (1989) used with a four class ice formulation reproduced the cloud top height, updraught structure and echo profile very well. To test the importance of ice physics upon thunderstorm development, several sensitivity tests were made removing the effects of the ice phase. All of these model clouds reached nearly 20 km, although simulations without the effects of ice had updraughts reduced from about 40 m s^{-1} to 30 m s^{-1}. The simulated convection was more sensitive to changes in environmental conditions and parameterised cloud dynamics. The strong intensity of the convection was largely accounted for by increasing equivalent potential temperatures due to diurnal heating of the surface layer. The vertical velocity and radar structure of the island thunderstorm has more similarity with continental rather than oceanic convection. Maximum vertical velocities, in particular are almost an order of magnitude greater than typical of oceanic convection. With the intense updraughts, even in the low shear environment, there is evidence for mesoscale circulations within the convection.

1. Introduction

The diurnal occurrence of thunderstorms over the myriad of islands comprising the Indonesian archipelago led Ramage (1968) to refer to the region as the "maritime continent". Studies by Krishnamurti et al. (1973), Janowaik et al. (1985) and Rasmusson and Arkin (1985) have shown that convection in this region is important in maintaining the Hadley and Walker circulations. Variations of the convective activity (Horel and Wallace, 1981) are related to the important El Niño-Southern Oscillation phenomena and can influence the behaviour of the subtropical jet on a daily basis (Lau et al., 1983). Rutledge et al. (1992) also provide evidence that the convection within this region is fundamentally important in maintaining the global electrical circuit.

In the absence of major disturbances, the diurnal island thunderstorms are the primary form of convection. Relatively few investigations of their structure have been undertaken. Houze et al. (1981) were the first to examine island convection and its mesoscale structure within the north-easterly monsoonal flow near Borneo. Williams and Houze (1987) and Keenan et al. (1989) further documented climatological characteristics and structure of thunderstorms within the region. The thunderstorms over Bathurst and Melville Islands near Darwin, Australia (12° S; 131° E), locally called Hectors, were shown by Keenan et al. (1990) to develop in a region of moderate Convective Avaliable Potential Energy (CAPE) in a low-to-moderate shear regime with high moisture. The storms were observed to aggregate or merge into mesoscale systems and form squall-like structures that moved off the islands. Data pertaining to the three dimensional structure of the convection, the rainfall production and information on the forcing of these systems were unavailable for this initial study.

Given the importance of these thunderstorms, a collaborative experiment called the Island Thunderstorm Experiment (ITEX), described by Keenan et al. (1989) was mounted by the Bureau of Meteorology Research Centre (BMRC), the Monash Centre for Dynamical Meteorology and the U.S. National Aeronautics and Space Administration (NASA) to study the characteristics and dynamics of these thunderstorms. The target area for this study was again the island thunderstorms that form over Bathurst and Melville Islands.

Simpson et al. (1993) described the rainfall and merging[1] characteristics of these systems on 9 days in 1988, one of which developed under a cirrus overcast. As in a previous study of mergers in south Florida (Simpson et al., 1980), about 90% of the total rainfall came from the large merged systems. However, the Hectors produced 3–4 times the rain volumes produced by the Florida systems, owing to larger areas and longer lifetimes.

The aim of this paper is to provide information on initial forcing and the three dimensional structure, evolution and characteristic mesoscale and convective scale features of one ITEX thunderstorm.

2. Data

The data for this study were collected as part of the ITEX field program on 22 November 1988. Figure 1 shows the location, topographic features and data network associated with ITEX. Melville and Bathurst Islands are located at the southeast extremity of the maritime continent and are approximately 50 km north of Darwin. The two islands are separated by a tidal channel. They are relatively flat (maximum elevation 121 m) with the most significant topographic feature being a shallow escarpment on the southern edge of both islands. The islands are covered with an open eucalypt forest with mangroves and saline flats around much of the coastal regions.

The ITEX observational network is described fully in Keenan et al. (1989). The primary observational tool employed in this study is the National Oceanic and Atmospheric Administration (NOAA) Tropical Oceans and Global Atmosphere (TOGA) Doppler radar located at Darwin. Operating characteristics of the radar are described in Table 1. Given the 50–150 km distance of the islands from the radar, the vertical resolution available from volume scans ranged from 2 km for most scans to 4 km for some scans. Range resolution was set at 1 km. The curvature of radar paths relative to the earth and the lowest radar tilt angles dictated that the minimum height of the radar beam over the island ranged from 0.3–0.5 km along the southern coast to 2–3 km along the northern coast. Considering the lack of sensitivity of the NOAA/TOGA radar to clear planetary boundary layer (PBL) features beyond 50 km (Keenan et al., 1991) and the above height restriction, it was impossible to discern clear air gust-front signatures associated with the island thunderstorm.

Table 1. *Operating Characteristics of the NOAA/TOGA Doppler Radar During ITEX*

Beamwidth	1.65°
Wavelength	5 cm
Pulse length	0.5–2.0 μs
Pulse repetition frequency	200–854 Hz
Minimum elevation	0.2°–0.5°
Maximum elevation	22.0°–25.0°
Sampling frequency	~5 minutes

[1] A formal definition of merging is given by Simpson et al. (1990). In this paper no dinstinction is made between their first- and second-order merging.

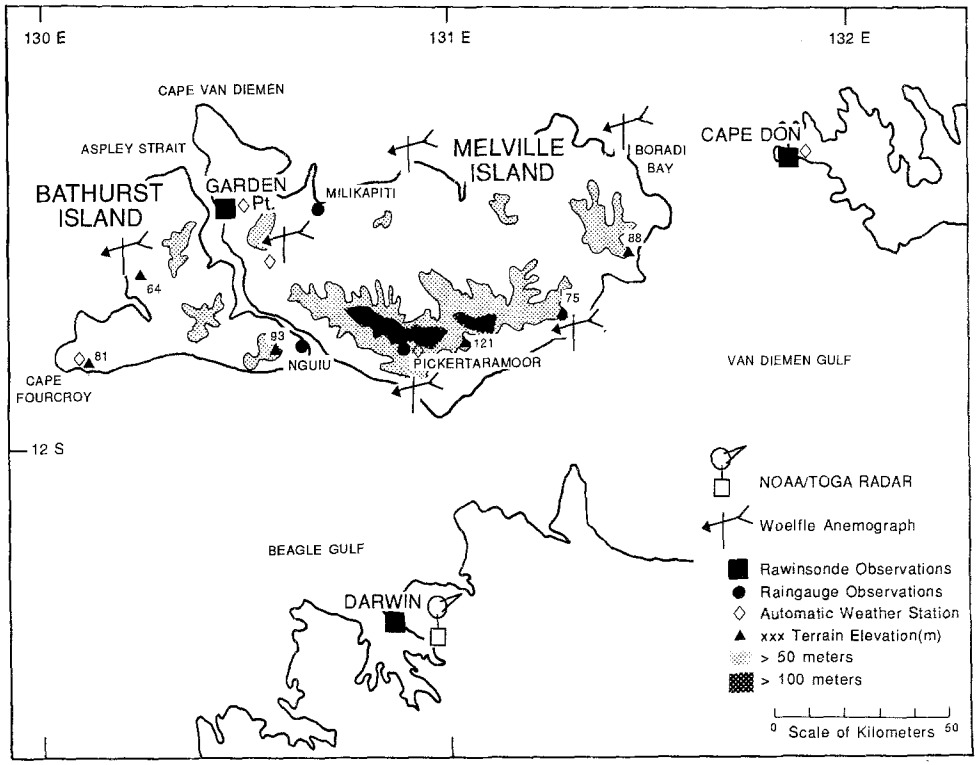

Fig. 1. Site for ITEX including observational network and topographic features

The radar data were edited to remove clutter, second trip echoes and resolve velocity ambiguities using the Research Data Support System software described by Oye and Carbone (1981). The data were then converted to cartesian grids with up to 1 km horizontal and 0.5 km vertical spacing using the bilinear method of Mohr et al. (1981).

3. Environmental Conditions and Evolution Overview

3.1 Synoptic Conditions

The tropical summer "wet" season in this region extends from November through April; it consists of periods of transition, break and monsoonal flow. The monsoonal flow typically consists of bursts of deep westerly flow from the surface to 400 mb with easterly flow above. The transition flow consists of low-to-middle level easterly flow with westerlies above. During these transitions diurnal forcing and land-sea contrasts dominate the production of precipitation, as described by Keenan and Carbone (1992). For the case presented herein, typical transition season conditions existed with generally easterly flow across northern Australia and the islands. Keenan et al. (1988) present evidence of a similar diurnal modulation of convective activity over Bathurst and Melville islands during the monsoon period, in which there is widespread stratiform precipitation and generally disturbed conditions.

3.2 Sounding Characteristics

The 1330 Central Standard Time (CST) Garden Pt (GP) sounding in Fig. 2 was obtained well in advance of the thunderstorm activity (see Fig. 4) and is considered the best available to represent the storm environment. A layered structure in the PBL is evident. The surface layer is superadiabatic with a marked decrease in moisture with height. Above this is a well-mixed adiabatic layer extending to near 850 mb (1.5 km) capped by a stable transition layer. The mixed layer is not as deep as found in continental locations and more representative of that found over the open ocean (Riehl, 1979). From 840 mb to 770 mb (2.3 km), there is evidence of a moist cloud layer which is capped by the trade wind inversion. The structure is typical of a PBL affected by broken shallow inversion-capped cumulus. Above the trade wind inversion is the characteristic dry region maintained by

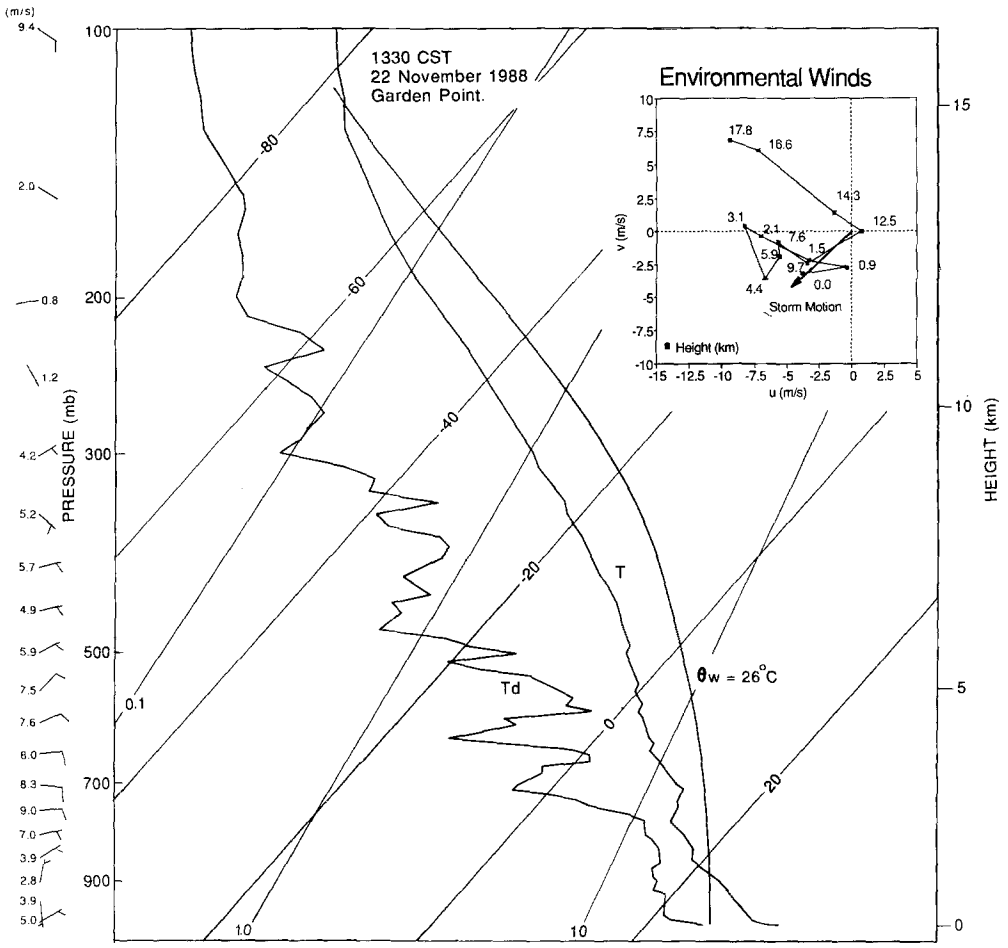

Fig. 2. The 1330 CST 22 November 1988 Garden Pt (GP) rawinsonde sounding. Moist adiabatic ascent through the LCL is indicated. Wind speed and directions are indicated to the left and in hodograph form in the top right hand corner

subsidence, which is potentially important for the evaporation of moisture and the driving of downdraughts. There is generally weak northeasterly flow at low levels with easterlies extending through the depth of the troposphere. The easterlies are a maximum near 3-km height and 18 km elevation, and at a minimum near 12-km height. The vertical shear profile is characterised by a low-level maximum towards the west below 3 km.

A comparison of 22 November 1988 GP sounding data with those representative of mean conditions for island thunderstorms (as given in Table 2 taken from Keenan et al., 1990) indicates the Convective Available Potential Energy (CAPE)[2] at 1330 CST was moderately high ($2780\,J\,kg^{-1}$) and the Convective Inhibition (CIN)[3] was near average ($-115\,J\,Kg^{-1}$). The bulk Richardson number[4] was high for this particular sounding, primarily as a result of the low shear conditions at 1330 CST. Based on the results of Weisman and Klemp (1982), the 22 November 1988 data indicate a dynamic regime

[2] CAPE as defined by Moncrieff and Green (1972), is the work done per unit mass on the enviroment by a buoyant air parcel as it rises from its level of free convection (LFC) to its equilibrium level (EL). The LFC was determined following Bluestein and Jain (1985) by lifting an air parcel having the average pressure-weighted potential temperature and mixing ratio weighted over the lowest 500 m.

[3] The CIN, as defined by Colby (1983) is the negative area or buoyant energy required to reach the LFC.

[4] The bulk Richardson number (R) is defined as $R = \text{CAPE}/(U^2/2)$ where $U = U_{3000} - U_{500}$, the density-weighted mean wind over the lowest 3 km minus that over 0.5 km. This definition of R follows that employed by Keenan et al. (1990). It does not use the 6 km level in defining shear as done by Weisman and Klemp (1982) as the natural shear layer is over the 0–3 km layer.

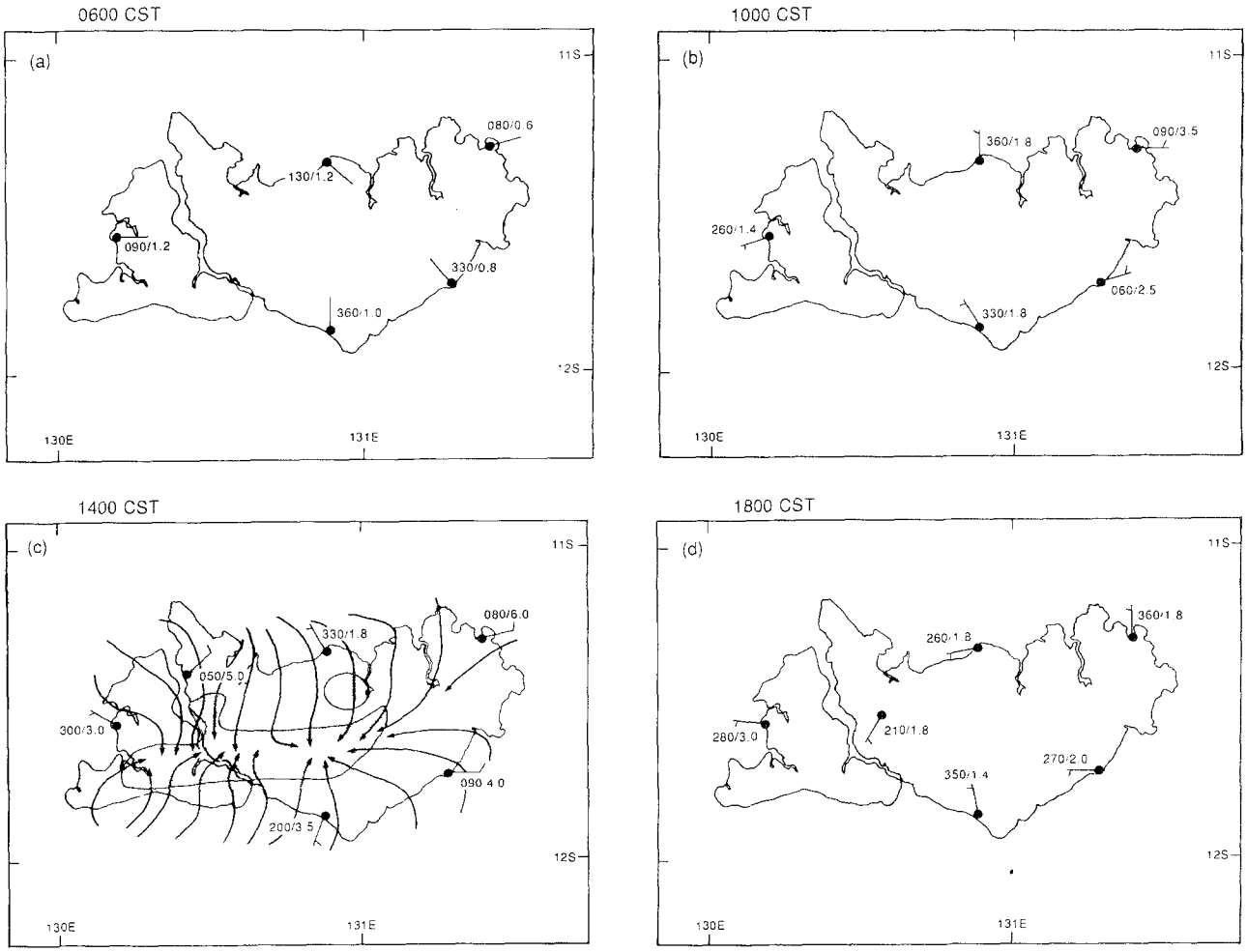

Fig. 3a–d. Evolution of sea-breeze flow on 22 November 1988 over Bathurst and Melville Islands as indicated by Woelfle anemograph data (a) 0600 CST, (b) 1000 CST, (c) 1400 CST and (d) 1800 CST. Each full barb represents 5 m s^{-1}, each half barb 2.5 m s^{-1}, arrows without barbs 1.25 ms^{-1} and calm condition are indicated by ●. A stream-line/isotach (m s^{-1}) analysis from a numerical simulation of the sea-breeze flow at 1330 CST, undertaken by Golding (1993), has been superimposed on the 1400 CST data. Areas where simulated flow is less than 2.5 m s^{-1} are stippled

in which unsteady multicellular growth is expected.

3.3 Evolution of Island Flow and Satellite-Observed Structure

Observations by Skinner (1990) showed a mean diurnal cycle of the land/sea-breezes over Bathurst and Melville Islands from the entire ITEX data set and deduced that this process resulted in the development of alternating low-level divergence/convergence averaged over the islands. The anemograph observations of near-surface flow over the islands for 22 November 1988 are shown in Fig. 3 with a numerically simulated flow from Golding (1993) for 1330 CST superimposed at 1400 CST. There are insufficient observations to analyse the inland penetration of the sea-breeze and its relation to the onset of convection, hence the use of the model simulation in Fig. 3.

At 0600 CST, all anemograph stations indicate flow consistent with a weak offshore-directed land breeze. By 1000 CST, most wind directions have reversed to be onshore and this persisted until 1800 CST when the flow again reverted to offshore. A sea-breeze circulation was therefore clearly evident on 22 November 1988.

The 1330 CST numerical simulation of the sea-breeze flow shows good agreement with the coastal anemograph data. The simulated flow at 1400 CST is available in Golding (1993) but differs little from that presented here. Over Melville Island, sea-breeze circulations from the northern, southern and eastern coasts have penetrated in-

Table 2. *Comparison of Garden Pt 1330 CST 22 November 1988 Sounding Data with Mean Island Thunderstorm Environmental Sounding Characteristics (Taken from Keenan et al., 1990) obtained from 0730 CST Darwin Sounding Data*

	Mean conditions	GP 1330 CST 22 November 1988
CAPE ($J\,kg^{-1}$)	1528	2783
CIN ($J\,kg^{-1}$)	−167	−115
Sub cloud shear ($\times 10^{-3}\,s^{-1}$)	2.5	1.2
Cloud layer shear ($\times 10^{-3}\,s^{-1}$)	0.25	−0.1
Bulk Richardson number	661	2447
Precipitable water (cm)	4.6	4.9
Saturation precipitable water (cm)	7.3	8.0
Tropospheric Humidity	0.63	0.62

land and have formed an east-west oriented convergence zone (stippled area shown in Fig. 3c) extending across both islands.

Satellite data at 1300 CST, as shown in Fig. 4a, indicate widespread shallow convection over both islands but with a tendency to be concentrated ~10 km inland of the northern coast and 5 km inland of the southern coast of Melville Island. At this time, less convective activity is evident in the centre of Melville Island with some evidence for north-west to south-east aligned bands of convection over the north-east of Melville Island. These bands are aligned roughly parallel to the surface to 700 mb shear i.e. they have the appearance of shear-driven longitudinal roll clouds.

At 1400 CST (Fig. 4b), the intensity of the convection has increased and is concentrated on the southern half of the islands, especially over Melville Island. On eastern Melville Island, there are north-west to south-east aligned bands and along the spine of Cape Van Diemen, there is clear evidence of a maximum in convective activity consistent with a sea-breeze convergence zone. By 1500 CST (Fig. 4c), the satellite imagery shows a mesoscale convective complex with deep convection over the central region of Melville Island with shallow convection completely suppressed. Deep convection is evident along the southern coast of Bathurst Island. These mesoscale convective systems have developed in the general area of sea breeze convergence indicated in Fig. 3c.

Prior to 1500 CST, it is assumed that the suppressed regions along the coastal zones are behind the leading edge of the sea breeze, which moves faster inland from the northern coasts than the southern coasts. This is consistent with model results presented in Fig. 3c. The low-level flow,

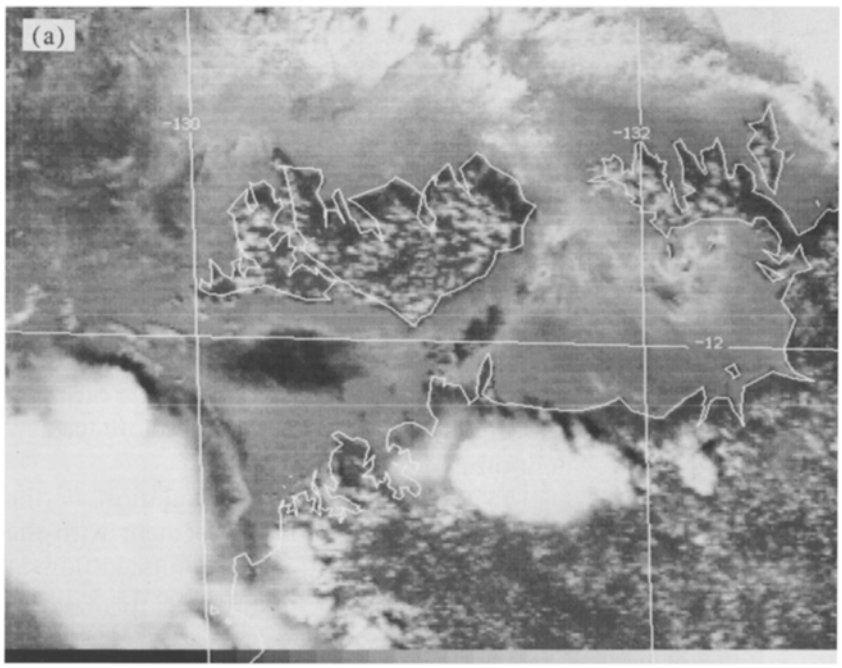

Fig. 4. GMS visual channel satellite observed cloud cover over Bathurst and Melville Islands at (a) 1300, (b) 1400, (c) 1500 CST 22 November 1988. Scale in kilometers shown at bottom of (c)

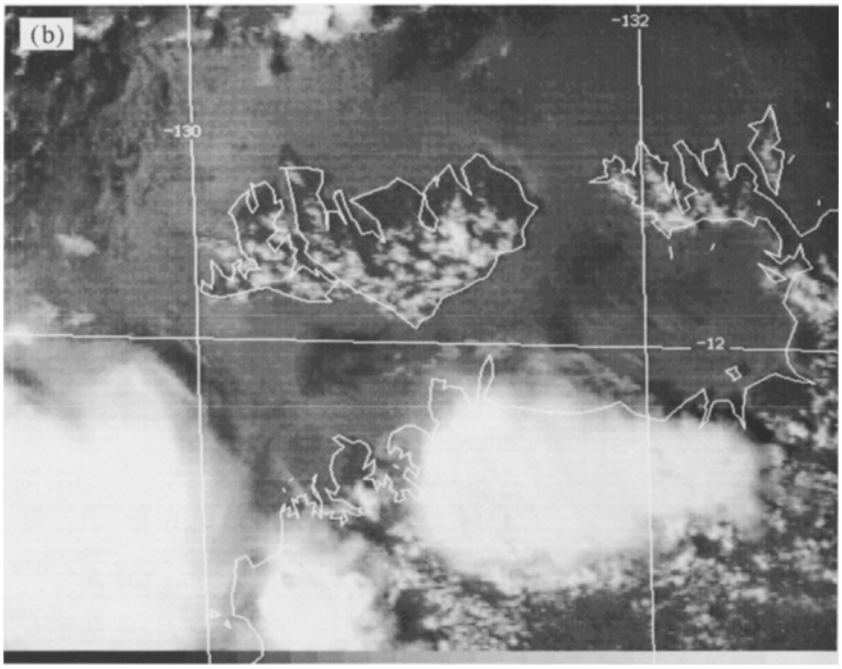

GMS VIS 22 NOV 88 1400 CST

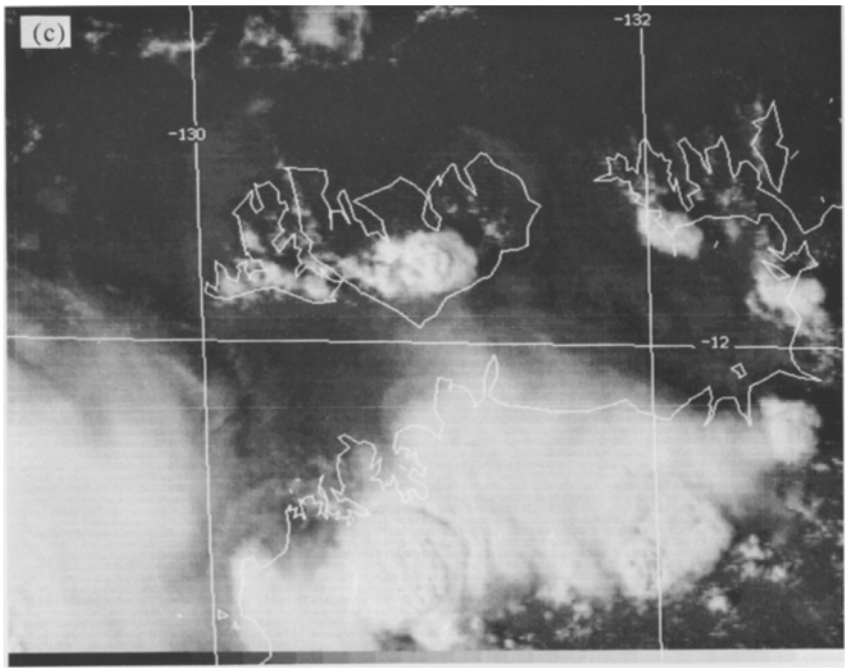

GMS VIS 22 NOV 88 1500 CST

Scale (km) 0 50 100

Fig. 4. (*Continued*)

which was from the northeast, would assist a southward-moving sea breeze and the existence of the escarpment region on the southern side of Melville Island may retard inland penetration of the sea breeze from the southern coast. A major area of PBL convergence associated with the interaction of sea breezes and local terrain was associated with the area of deepest convection over the southern parts of Melville and Bathurst Islands.

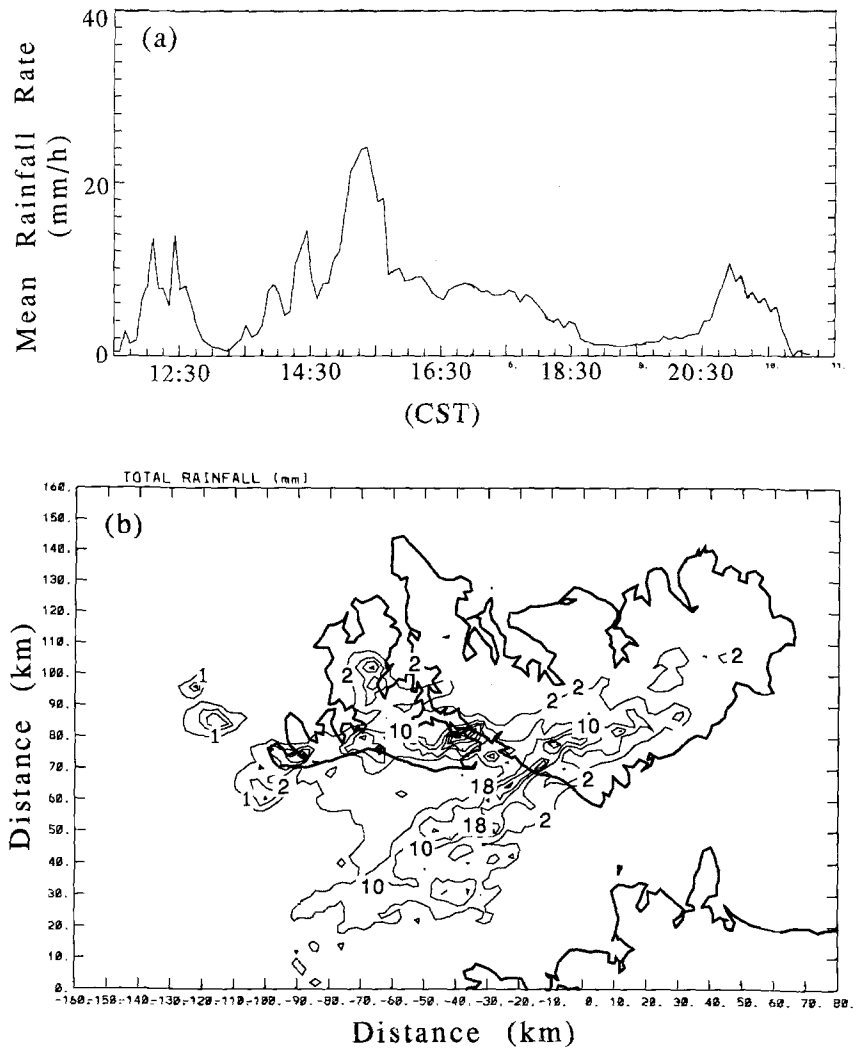

Fig. 5. Time series of radar-derived (a) storm-mean rainfall rate (rain rate averaged over total echo area). The early double peak between 12:20 and 12:40 was due to early mergers in the southwest portion of Bathurst Island and (b) accumulated rainfall (mm) observed over Bathurst and Melville Islands on 22 November 1988

3.4 Rainfall Production

The rainfall production from the island thunderstorm of 22 November was estimated from the NOAA/TOGA radar data calibrated by gauge data as described by Simpson et al. (1993). As shown in Fig. 5a, after an initial phase commencing at 1131 CST associated with the complex E1 over Bathurst Island (see Fig. 6a), the most active period of rainfall occurred between 1500 CST and 1530 CST, when the mean rainfall rate was estimated to reach $\sim 24\,\text{mm h}^{-1}$. The area covered by rainfall tripled from $500\,\text{km}^2$ to reach $1500\,\text{km}^2$ over this period.

The accumulated rainfall shown in Fig. 5b, indicates that the precipitation was concentrated on the southern half of Bathurst and Melville Islands and in a major southwest-to-northeast aligned band that extended 100 km offshore. The island thunderstorms not only produce rainfall over the islands, but sometimes results in a considerable amount of rainfall over the surrounding ocean.

4. Mesoscale Structure of the Island Thunderstorm

4.1 Overview of Radar Structure

The radar-observed evolution of the 22 November 1988 island thunderstorm complex is shown in Fig. 6. At 1337 CST, a few cells are evident over both islands. By 1427 CST (Fig. 6b), new cells had developed over the centre and southern coast of Melville Island. Merging of cells farther to the east resulted in a northwest-to-southeast oriented band (L1). The cells from which L1 originated moved inland from the Boradi Bay region and were evident at 1337 CST (Fig. 6a and at 1400 CST in Fig. 4b). At 1533 CST (Fig. 6c), apart from a few isolated cells, the island thunderstorm

is dominated by a major east-to-west oriented mesoscale complex (L2) aligned parallel to the 700 mb (about 3 km level) flow and located within the main seabreeze convergence zone (see Fig. 3c). As shown in Figs. 5a and 8, the growth of L2 resulted in a rapid increase in precipitation production from the island thunderstorm simultaneously with a rapid accleration of its vertical growth.

At 1633 CST (see L3 in Fig. 6d), the island thunderstorm complex reoriented to a northwest-to-southeast alignment with active convection on the southwestern flank and a developing stratiform region trailing to the northeast. The leading convective line is almost parallel to the surface-to-700 mb shear vector (see hodograph in Fig. 2) and is becoming perpendicular to the 700 mb flow. Figure 5 shows that after 1510 CST most of the rainfall occurred at rates less than 10 mm h^{-1} and was predominantly stratiform.

The motion of the main system evolving from Melville Island is summarized in Fig. 7. Up to

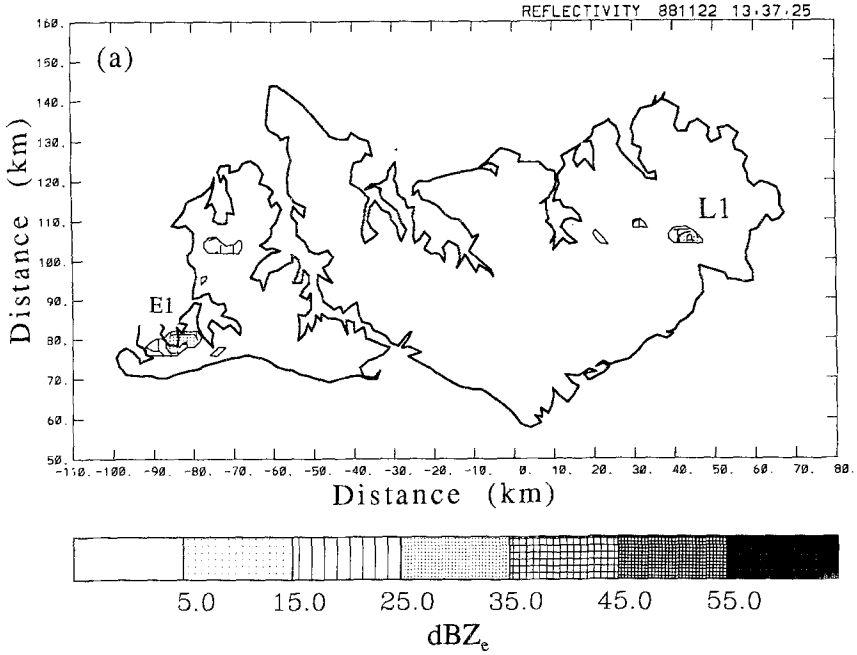

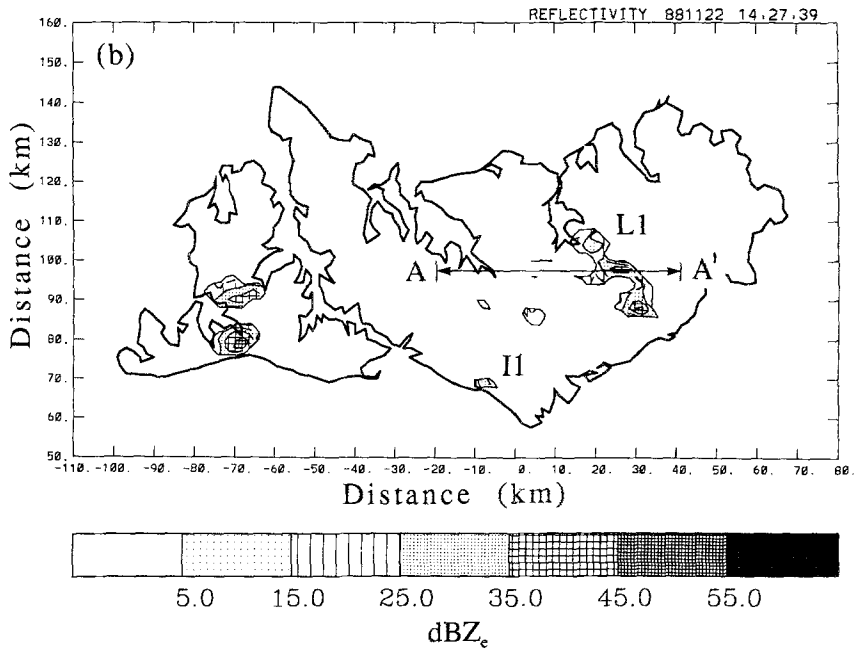

Fig. 6. Radar observed structure of island thunderstorms over Bathurst and Melville Islands at (a) 1337 CST, (b) 1427 CST, (c) 1533 CST, (d) 1633 CST and (e) 1733 CST. Data plotted at 2 km resolution and derived from 0.5° elevation tilt. See text for details

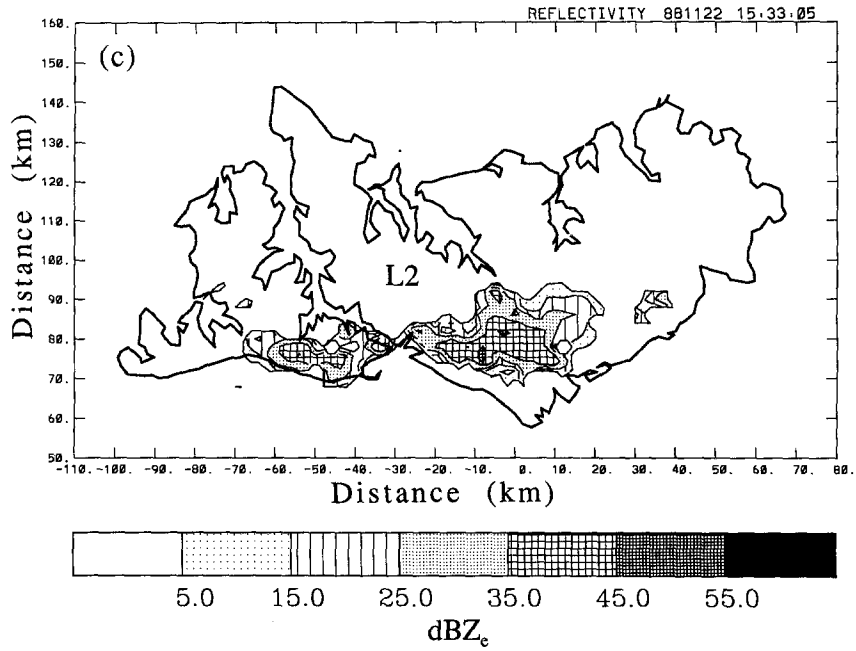

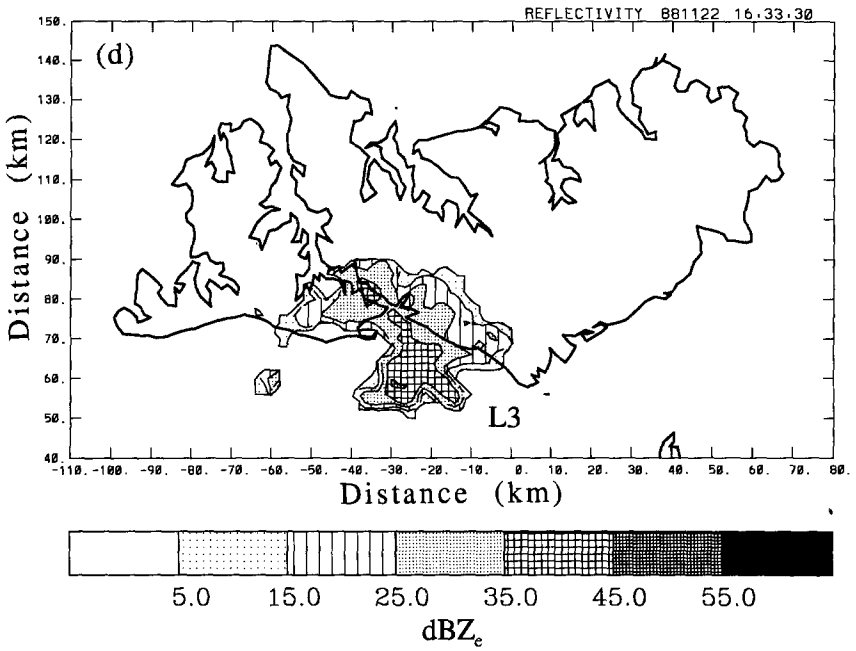

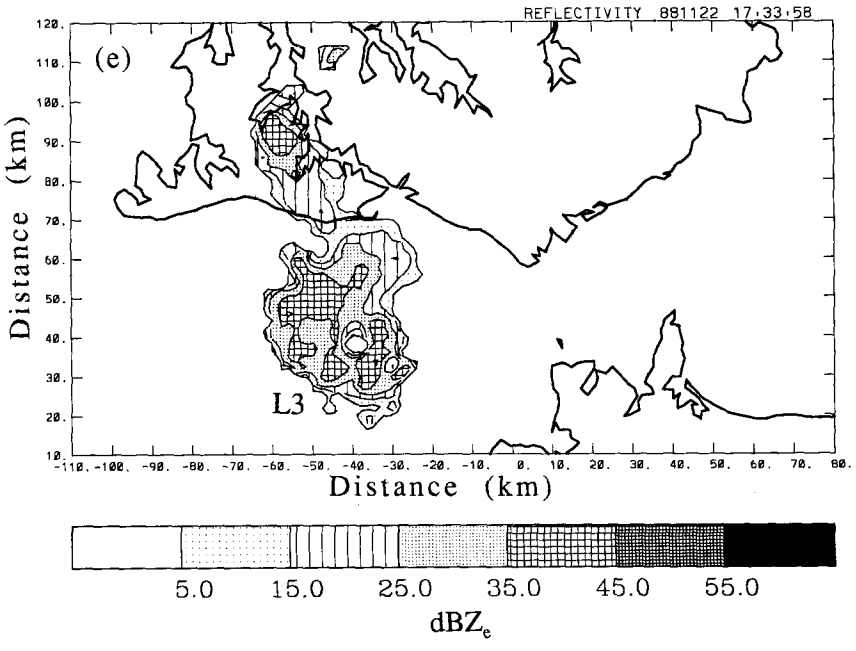

Fig. 6. (*Continued*)

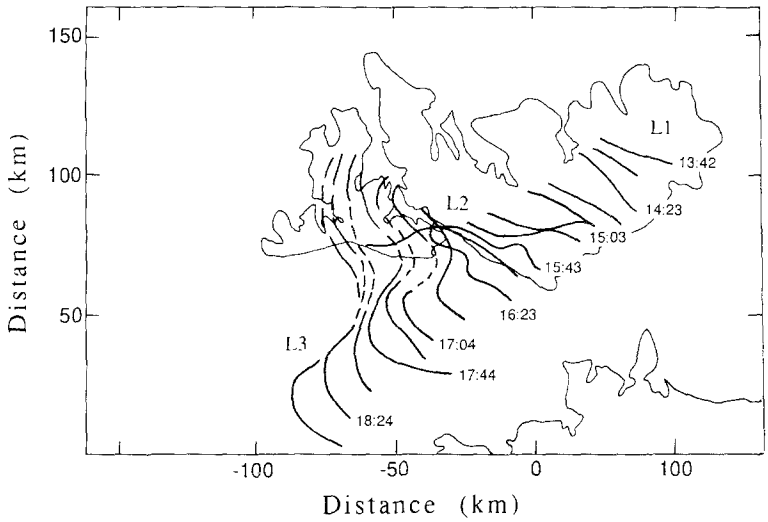

Fig. 7. Isochrones at 20 minute intervals through the leading edge of 35 dBZ_e – 45 dBZ_e echoes indicating the location of the main mesoscale systems (L1–L3) associated with the 22 November 1988 island thunderstorm. Times are CST

1500 CST, the dominant Melville Island complex, L1, which was first detected at 1337 CST moves in from the north-east from 48° azimuth at 7.5 m s^{-1}. At 1503 CST, L1 merges with L2, a pre-existing merged complex formed at 1454 CST from (a) developing convection over central Melville and (b) convection originally detected over Bathurst Island. The identity of L1 is lost within the initially east-west aligned merged complex L2. The eastern portion of L2 continues to move southwestward with time after 1500 CST, forming the southern lobe of the complex L3 by 1633 CST (Fig. 6d). This section of L2/L3 moved from 50° azimuth at 7.6 m s^{-1} over the period 1500–1845 CST, remarkably similar to the motion of L1. After 1630 CST, the northern extension of L3, which was originally the western half of L2 over Bathurst at 1530 CST (Fig. 6c), also moves to the southwest but more slowly and zonally (from 60° at 4.3 m s^{-1}) than the southern segment of L3. During this latter period, the storm was essentially aligned perpendicular to the 700 mb flow. Overall, the island thunderstorm complex moved from 50° azimuth at 6.6 m s^{-1}.

The mean surface to 700 mb pressure-weighted flow from the GP sounding was from azimuth 75° at 4.2 m s^{-1}. The mean, pressure-weighted surface-to-700 mb flow at 1330 CST over the entire ITEX network (obtained from soundings at GP, Darwin and Cape Don) was from 49° azimuth at 3.7 m s^{-1}, which is reasonably consistent with the direction of storm motion.

The observed life cycle of this storm from initially independent cell growth, the merging of convection to an east-west oriented mesoscale system, and the subsequent reorientation with the development of a squall-like system is consistent with that observed in cases studied by Keenan et al. (1990) and with most of the cases described in Simpson et al. (1993).

The goal here is to describe the observed evolution, three dimensional convective scale and structure of a typical system. Whilst significant rainfall was observed from E1 (see Fig. 5a and Fig. 6a) over Bathurst Island, the period of maximum rainfall production and evolution of the main convective complex occurred over Melville Island from 1445 CST to 1540 CST. This period of maximum rainfall production (see Fig. 5a) has been selected for study. The discussion will concentrate on features relating to:

1. *Initial cells.* Short-lived initial precipitating cells existing independent of merger prior to 1454 CST.
2. *Merger and rapid growth phase.* Period of most intense precipitation associated with development of an east-west oriented merged complex bridging across both islands, with highest vertical development followed by reorientation to a system aligned almost perpendicular to the low-level flow. Period 1454 CST to 1530 CST.
3. *Mature squall line phase.* The mesoscale convective system aligned approximately perpendicular to the low-level shear with a leading convective edge and trailing stratiform region. Period after 1530 CST.

4.2 *Initial Cells*

4.2.1 Shallow Non-Precipitating Convection

Preceding the radar detection of the first precipitation echoes is a period dominated by shallow cumulus convection. Between 1030 CST and 1330 CST, during the shallow convection, modifications to the GP soundings consisted of a deepening, warming ($\sim 1\,^{\circ}C$), and moistening ($1-2.5\,g\,kg^{-1}$) of the mixed layer, moistening of the cloud layer ($\sim 1-2\,g\,kg^{-1}$) and a slight weakening of the trade wind inversion (not shown).

Some suggestion of cloud streets along the low-level shear is evident in Fig. 4a and 4b. Cloud street organisation has been associated with wind profiles showing a jet-type maximum near cloud base (Kuettner, 1971) but the accompanying windspeeds are commonly stronger in the PBL than found here. Weak winds combined with terrain effects apparently reduce the occurrence of persistent cloud streets over Melville and Bathurst Islands.

4.2.2 Independent Precipitating Cells

These randomly occurring cell-type radar echoes, for example I1 shown in Fig. 6b, are short-lived (10–15 min) and shallow. The vertical structure of these cells is summarised in Fig. 8 in a time-height Lagrangian coordinate system moving with I1. In this case, the initial echo height was from 2–4 km, well below the freezing level at 5 km, indicating that precipitation was produced most likely as a result of "warm rain" processes. Maximum equivalent reflectivity was $\sim 20\,dBZ_e$ at a height of ~ 2 km. Doppler data (not presented) do not show evidence of a strong radial convergence (divergence) with this cell, implying weak vertical motions. Maximum echo top from I1 was 6 km. At this time, no source of ice particles from deep convection was close enough to explain the production of precipitation through ice settling and a melting processes.

4.2.3 Organised Precipitating Cells

The cells within L1 in Figs. 6a–b, forming at 1337 CST on the northeast corner of Melville island, are an example of initial linear organization quite different from non-precipitating cloud strees. The merging of raining cells into an organised system is evident and is almost certainly associated with gust-front outflows. Line L1 has the appearance of a multicellular storm with new cells forming $\sim 6-10$ km downwind of the older cells.

The vertical structure of L1 along the cross-section AA′ (see Fig. 6b) shown in Fig. 9 is very different from I1. The maximum echo top was 14 km ($T = -70\,^{\circ}C$), indicative of a storm in which ice-phase processes were now important in

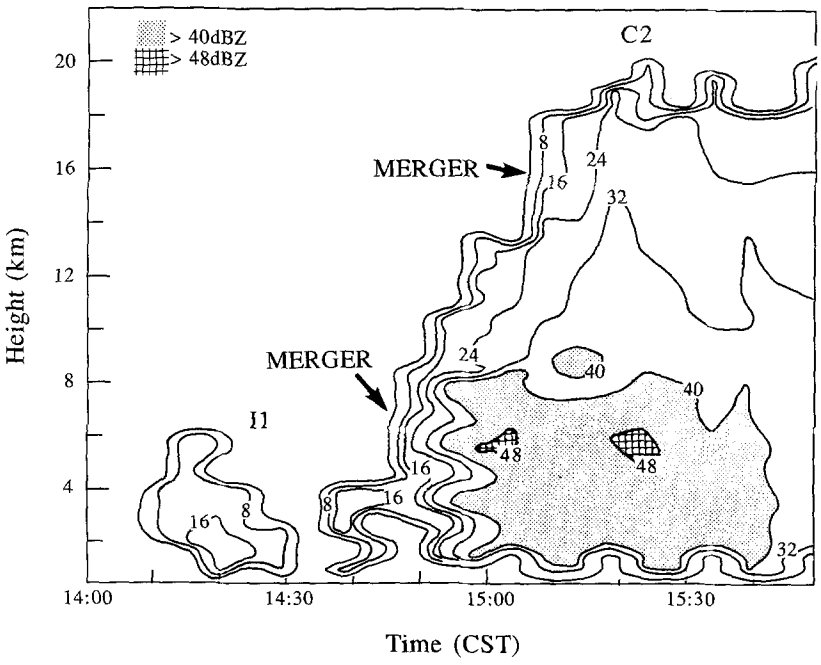

Fig. 8. Time height radar reflectivity (dBZ_e) section of echo I1 (to 1430 CST) and then C2 (after 1440 CST). Areas with reflectivity $> 40\,dBZ_e$ are stippled. Times of significant mergers are indicated. Note I1 and C2 represent separate systems. Location of I1 is indicated in Fig. 6b and location of C2 is given in Fig. 10a–b

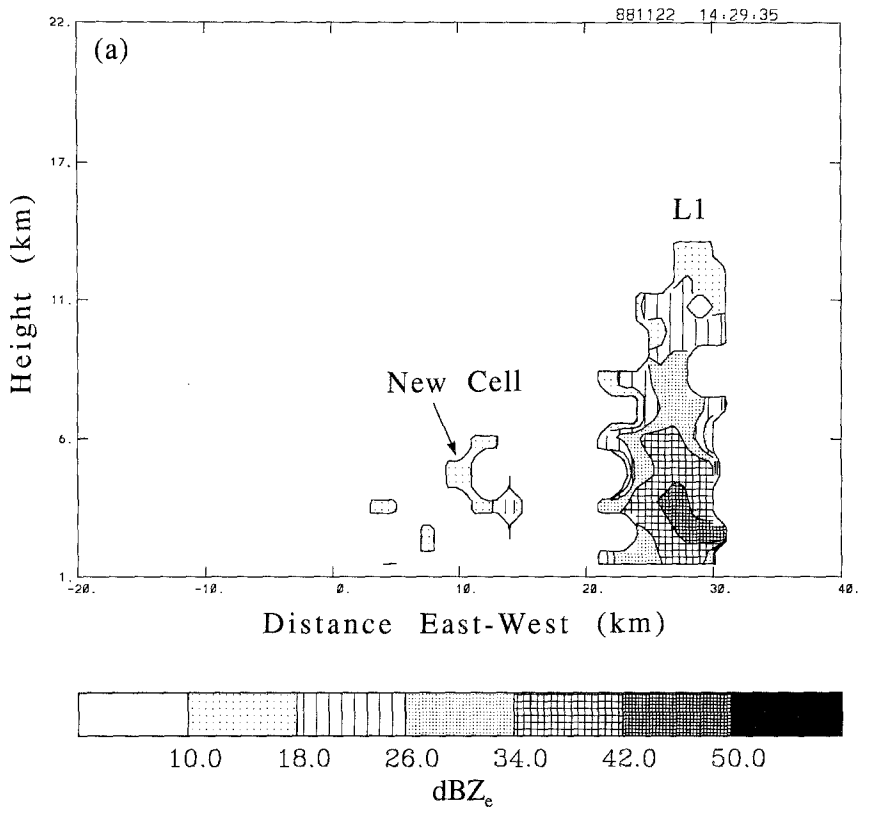

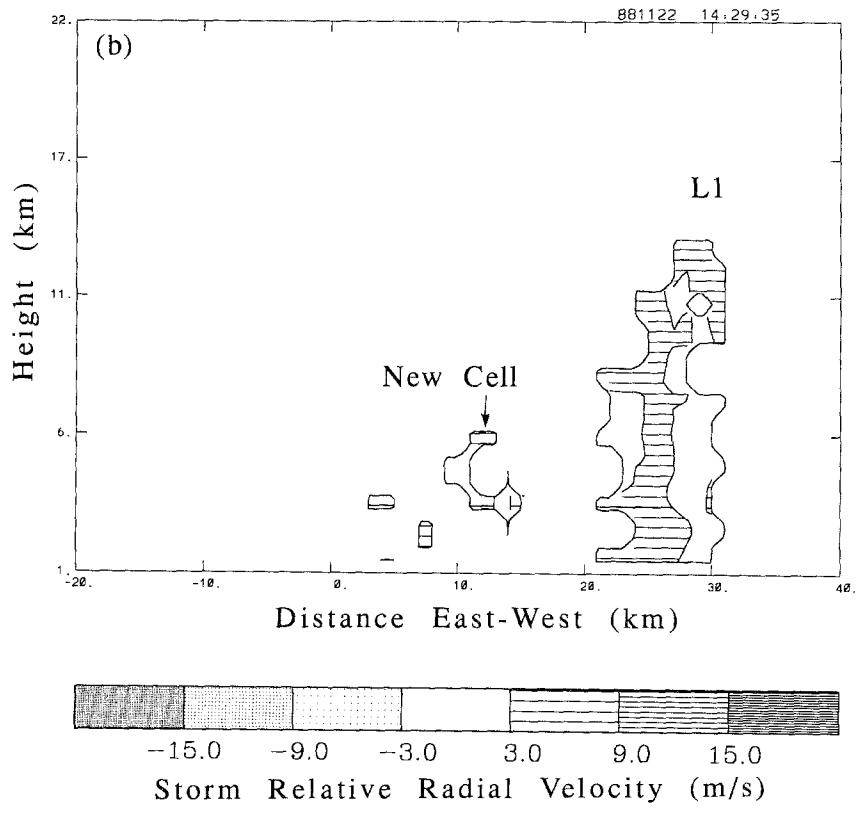

Fig. 9. East-west cross-section AA′ (see Fig. 6b) through L1 at 1429 CST. (a) Reflectivity (dBZ_e) and (b) storm-relative Doppler derived radial motion field ($m\,s^{-1}$). Negative motion is towards the radar. Storm motion is from 45° at $7.1\,m\,s^{-1}$

the production of hydrometeors. The motion[5] detected by the Doppler radar includes a deep and vertically-erect (sloping $\sim 70°$ from the horizontal) area of radial flow away from the radar. This motion is consistent with a front-to-rear (south to north) updraught. Maximum echo strength (42–50 dBZ_e) is still concentrated at ~ 3 km height, well below the freezing level and at the rear of the inferred updraught. This suggests precipitation fallout to the rear of the updraught. This arrangement is effective for cold-pool production and development of a multicellular storm. A narrow tower with weak echoes extends above 5 km height and is concident with the updraught. In this case, a mixed-phase region probably extends from 6–10 km. Echoes consistent with new cell generation are evident near $x = 10$ km. The height of the first radar echo (3 to 6 km) is consistent with warm rain processes playing an important role in the initial production of precipitation.

The most likely cause of initiation of deep, penetrative convection is from rain cell development, downdraught outflows and merging along the sea-breeze front. Examination of the sea-breeze front near Darwin shows that a typical depth is 1–1.5 km. A lifting of 1.5 km would certainly provide the impetus for a parcel to reach the LFC in the GP sounding (see Fig. 2b) and hence realise the potential for deep convection. Associated with this deeper convection and precipitation is the development of evaporatively cooled downdraughts, which form a westward-propagating cold pool on which new cells can be initiated ahead of the storm. Examination of automatic weather station wind, temperature and pressure data obtained on Melville Island offers observational evidence for the existence of these cold pools. Hence the multicellular, long-lived mesoscale structure of these storms are distinctly different from the short-lived, shallow systems discussed previously. Section 5d raises questions relevant to the early initiation of deep convection from a modelling viewpoint. The evolution of this initial convection has many similarities to cells modelled over the Florida peninsula by Nicholls et al. (1991). There small-scale cells (heights 1–4 km) developed between converging sea-breeze fronts with the strongest convection concentrated along the leading edge of the sea-breeze front. These initial shallow cells resulted in a moistening of $\sim 1\,g\,kg^{-1}$ between 1–3 km above the surface, as observed here. Typical vertical motions for the shallow cells were $\sim 1\,ms^{-1}$, consistent with the observations presented. Suppression of the shallow convection was also noted (see satellite data at 1500 CST in Fig. 4) with the onset of deep convective activity. This suppression of the shallow cells was associated with compensating subsidence surrounding the deeper convection. Compensating subsidence is similarly manifested in the clear rings surrounding heated islands with intense day-time convection (Malkus, 1955).

4.3 Rapid Growth Phase

The period 1454 CST to 1540 CST coincided with the most rapid vertical development as well as growth in areal coverage and in the amount of precipitation. During this period, as shown in Fig. 10, a significant merger occurred between L1 and line L2. This was followed by a reorientation of the main convection and by 1540 CST continued motion to the southwest of a multicellular squall-like storm along the southeast of L3. The origin[6] of L2, like L1 cannot be ascertained with the data available; however, as shown in Fig. 3, the mergers occurred in a general area of enhanced low-level convergence associated with the sea-breeze circulation.

The structure of the thunderstorm during this rapid developing phase will now be investigated using a series of vertical cross sections.

4.3.1 Initial Merger Phase at 1454 CST

At 1454 CST, as shown in Fig. 10a, two major lines L1 and L2 are evident with cell C1 developing between them. The onset of bridging is evident

[5] In Fig. 9 and Figs. 11–15, a storm motion has been subtracted from the Doppler-derived radial motion fields presented. The storm motion values are indicated in the captions.

[6] Possible explanations include 1) Development on a sea-breeze front penetrating inland from the southwest coast of Melville Island. 2) Initiation on outflow from L1 or interaction between the above sea-breeze front and outflow from L1. 3) Gravity wave excitation of convection downstream of L1 by the mechanism proposed by Balaji and Clark (1988). 4) Some form of orographic enhancement of convergence on the north side of the escarpment region of south Melville Island.

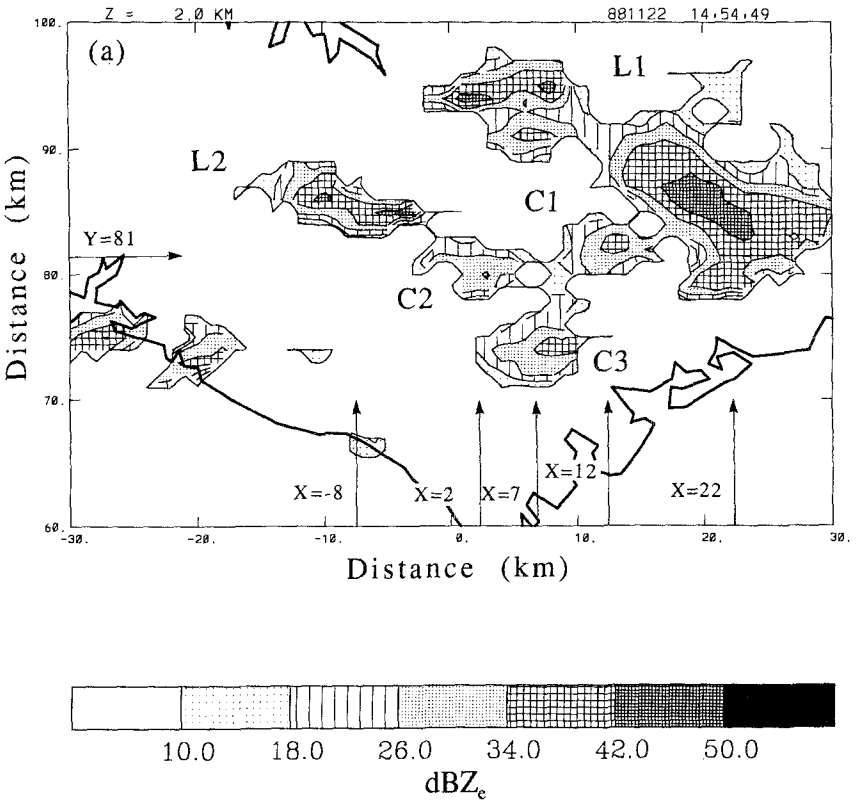

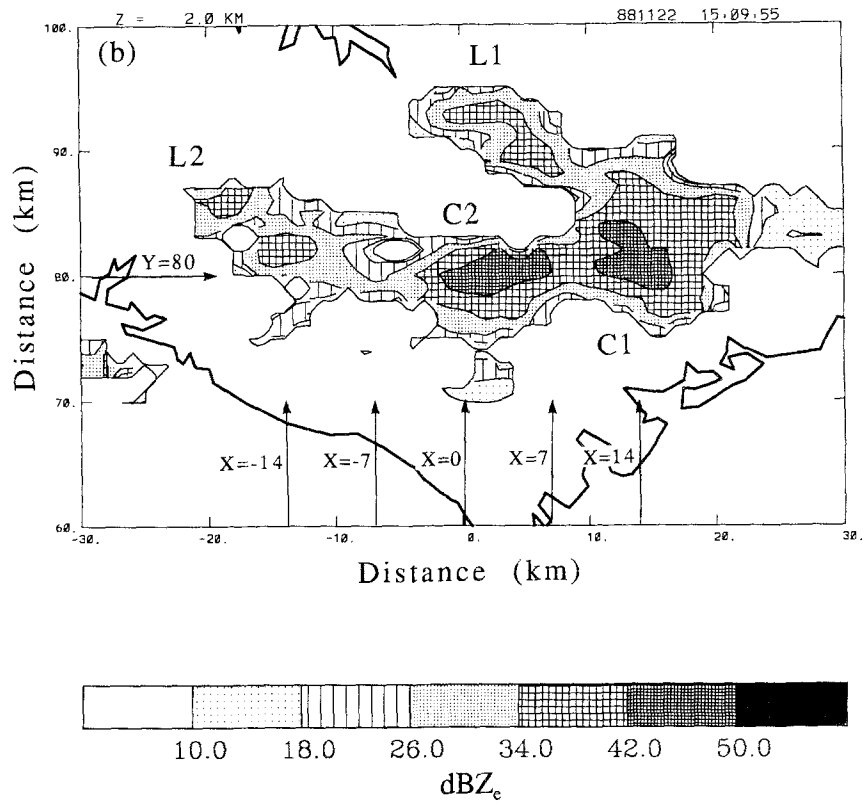

Fig. 10. Radar observed evolution of 22 November 1988 Melville Island thunderstorm complex at (a) 1454 CST, (b) 1509 CST, (c) 1525 CST and (d) 1540 CST. Each image is a CAPPI of equivalent reflectivity (dBZ_e) at 2 km height with 1 km horizontal resolution. Direction of vertical cross-sections presented in Figs. 11, 12, 13 and 15 are indicated

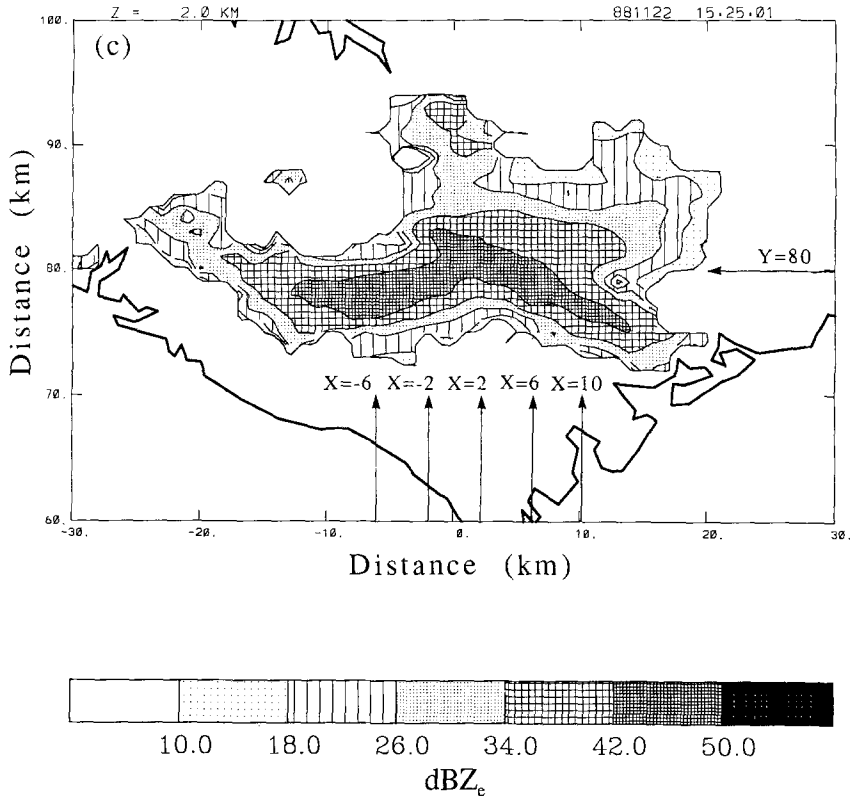

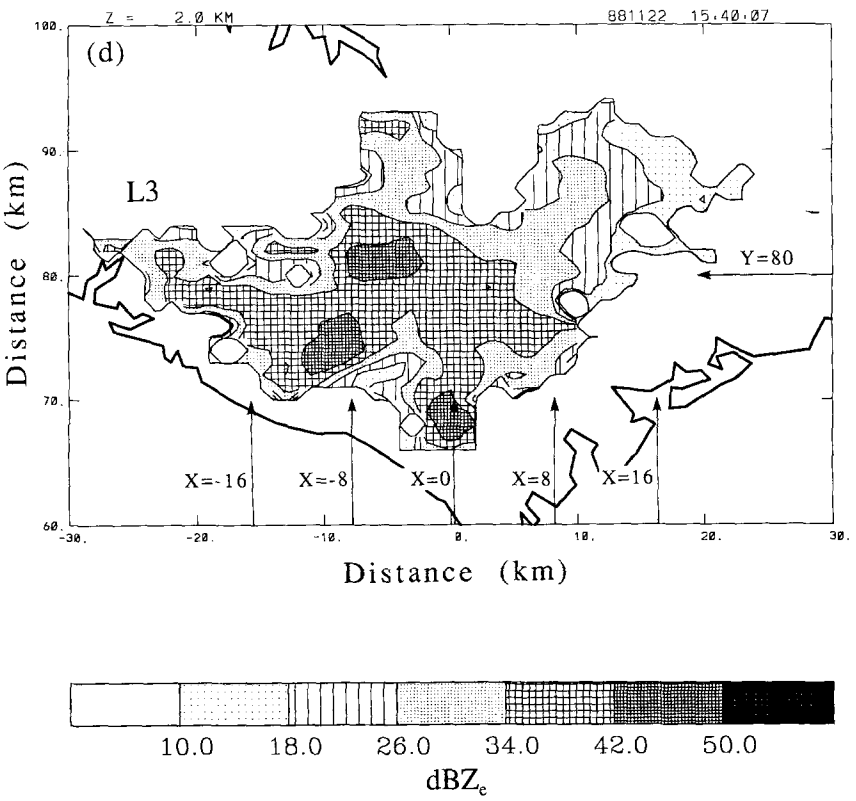

Fig. 10. (*Continued*)

between C2, C1 and L1. A time-height section of the cell C2, the dominant cell formed in this merger process, is shown in Fig. 8. The initial C2 echoes were detected at 1435 CST between 1 and 4 km height. Weak radial motion away from the radar between 2 and 3 km height (not shown) and divergent flow (not shown) near 4 km height suggests inflow to an updraught in the developing cell with outflow above.

At ~1445 CST, coinciding with the merger of the cells within L2, a rapid growth phase commenced. Cell C2 grew from 4 km to 8.5 km (T = 0 °C to −24 °C) within 4 minutes (rise rate of echo top ~19 m s^{-1}) with little rain reaching the surface. The Doppler data show radial motion away from the radar consistent with a front-to-rear updraught. Assuming this growth can be modelled as a thermal, as suggested by data in Fig. 13, and by observational studies (e.g. Scorer and Ludlam, 1953; Malkus, 1954; Malkus and Scorer, 1955) and numerical modeling (Simpson and van Helvoirt, 1980; Turpeinen and Yau, 1981; Simpson and McCumber, 1982; Ferrier and Houze, 1989) of tropical convection, the ratio of the cloud-top rise rate to maximum interior vertical velocity should be somewhere between 1.5 and 2.3 (Woodward, 1959). This implies maximum vertical velocities within the storm between 28 m s^{-1} and 43 m s^{-1} if the echo top is indicative of cloud top. It should be noted that Hallett et al. (1990) estimated cloud top rise rates of 30 m s^{-1} from time lapse movies of a 1989 island thunderstorm. If correct, this implies maximum in-cloud updraughts in the range from 45 m s^{-1} to 70 m s^{-1}.

An east-west cross-section along Y = 81 km at 1454 CST (Fig. 11a–b) where the main east-west oriented system appears shows bridging between C2 and C1 is at a maxium near 3 km height. It

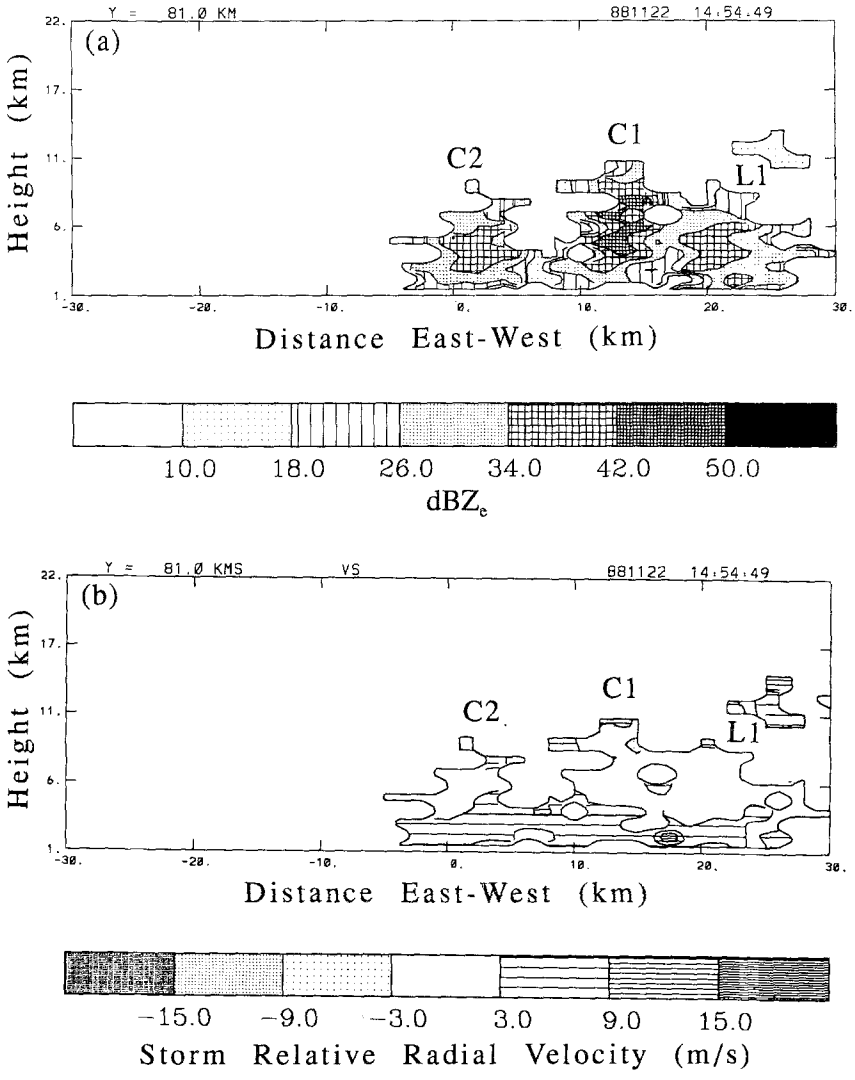

Fig. 11. Vertical cross-sections through island thunderstorm at 1455 CST. (a) Reflectivity field (dBZ$_e$) along y = 81 km, (b) storm relative radial motion (m s^{-1}) field along y = 81 km, (c) north-south reflectivity (dBZ$_e$) cross-sections at locations indicated and (d) north-south storm-relative Doppler-derived radial motion fields (m s^{-1}) at locations indicated. Arrows give sense of radial motion field in (d). Cross-section directions and cell locations are shown in Fig. 10a. Storm motion is from 34° at 5.9 m s^{-1}

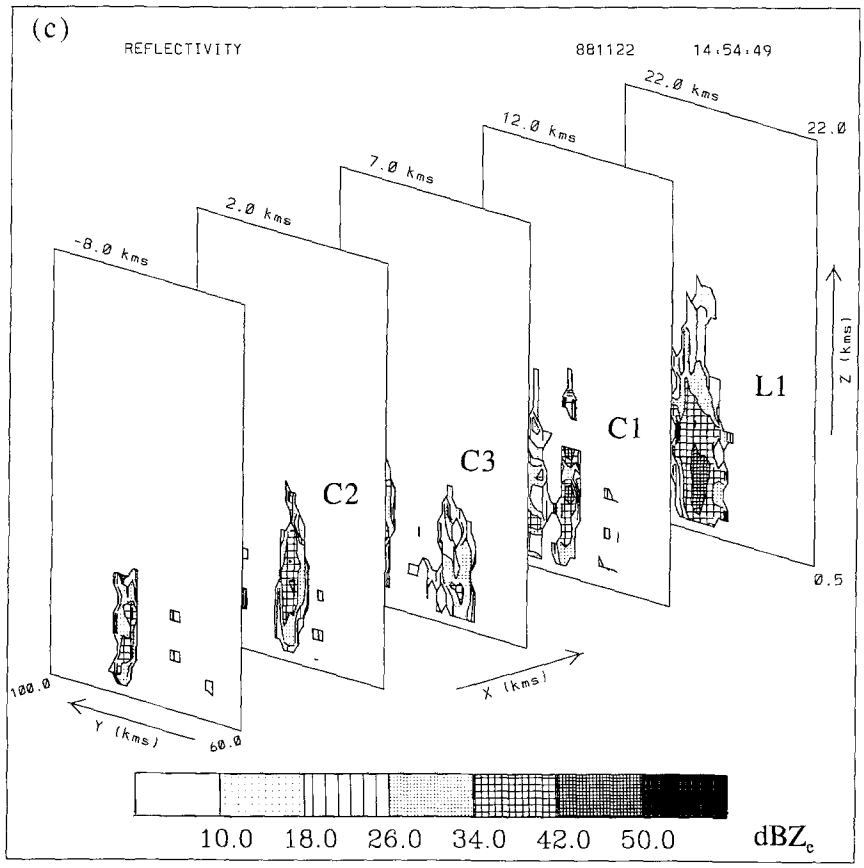

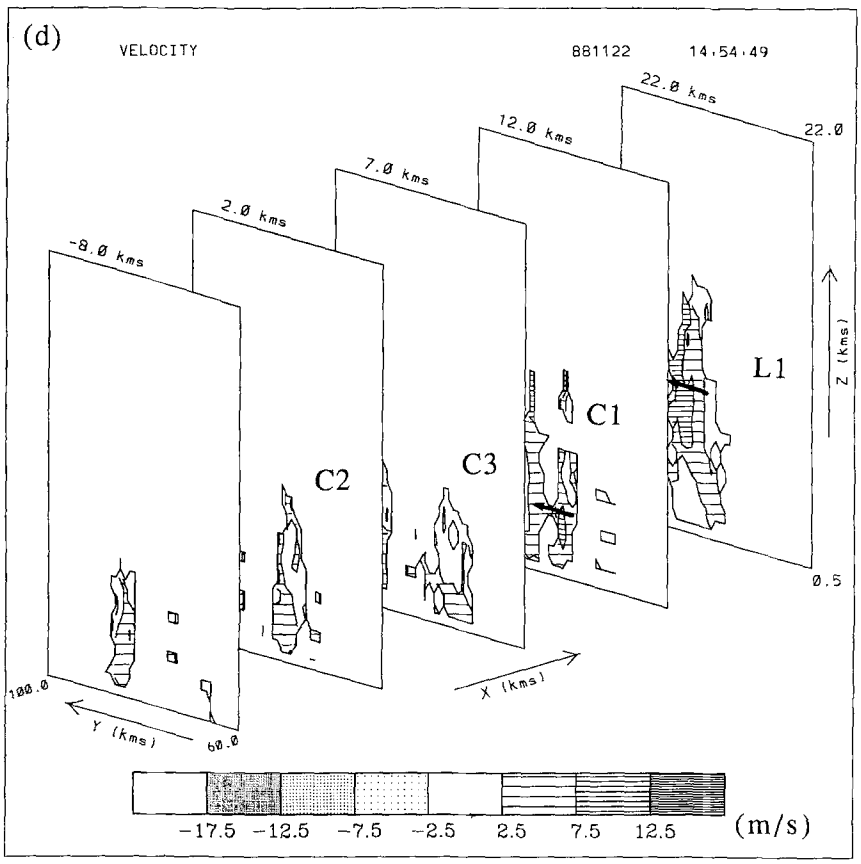

Fig. 11. (*Continued*)

also shows that the merger of C1 and L1 is well established with $>26\,dBZ_e$ echoes extending from 4–7 km height. Doppler motion indicates motion radially away from the radar up to 5 km, implying an updraught feeding the bridges from the south. The north-south cross-sections, as shown in Figs. 11c–d indicates the deepest convection at this time was within L1. Consistent with the data presented previously, L1 was ~17 km keep with radial motion away from the radar consistent with a deep front-to-rear updraught from the south but now sloped ~30° from the horizontal. By 1454 CST, the updraught had a much greater tilt than observed at 1430 CST in Fig. 9. Echoes from C1 were up to ~11 km deep.

At about 1505 CST, there was a second rapid growth phase coinciding with the merger of the bands L1 and L2. At this time, as the time height section in Fig. 8 shows, the maximum echo top of C2 increased from 13 km to 18 km within 6 minutes implying a rise rate of $\sim 14\,m\,s^{-1}$. Again, assuming a thermal-like turret, this would suggest maximum interior vertical velocities between $21\,m\,s^{-1}$ and $32\,m\,s^{-1}$.

4.3.2 East-West Oriented Merger Stage

At 1509 CST, as shown in Fig. 10 b, an east-west oriented mesoscale complex was produced by the merger of cells C1, C2 and lines L1 and L2. The east-west cross-section through $y = 80$ km given in Figs. 12a–b shows that this merged complex is dominated by cells C2 and C1, which reached heights of 18 km and 16 km, respectively. Maximum echo strength is consistently below the 7–8 km level, where 42–50 dBZ_e echos extended to 7 km

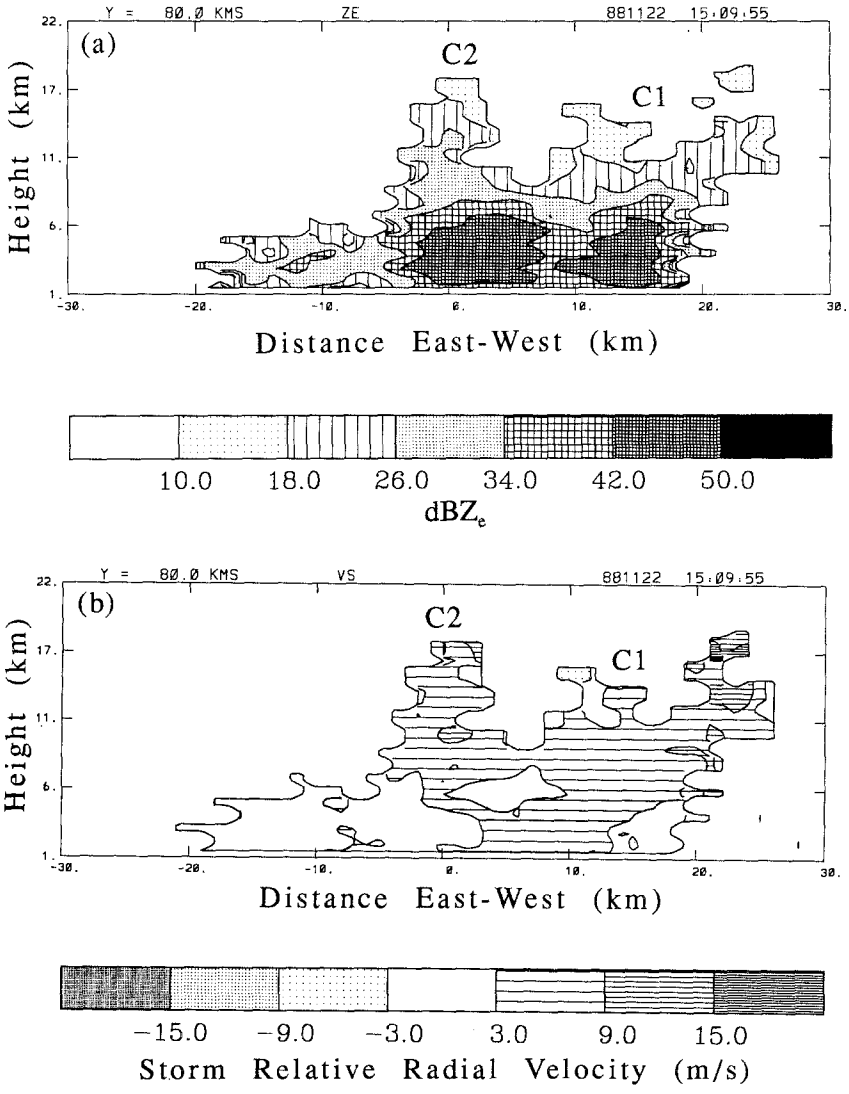

Fig. 12. Vertical cross-sections through island thunderstorm at 1509 CST. See Fig. 11 for details. East-west cross-section is along $y = 80$ km in Fig. 10b. In (c) arrows denote location of constriction and weak echo region (WER). Storm motion is from 27° at $4.9\,m\,s^{-1}$

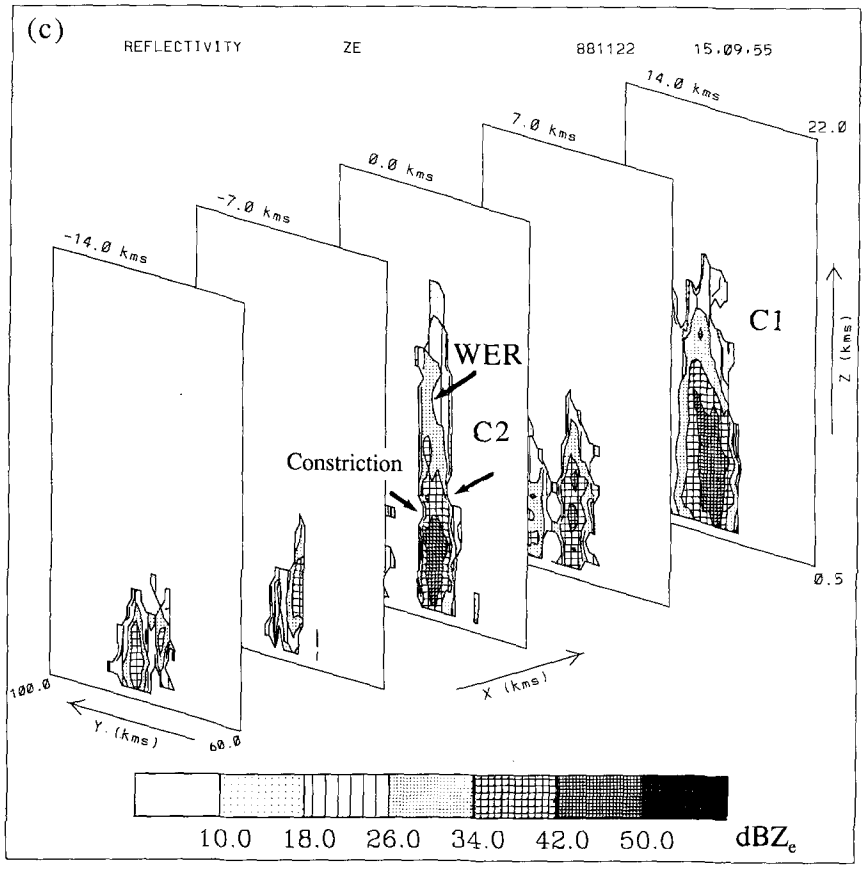

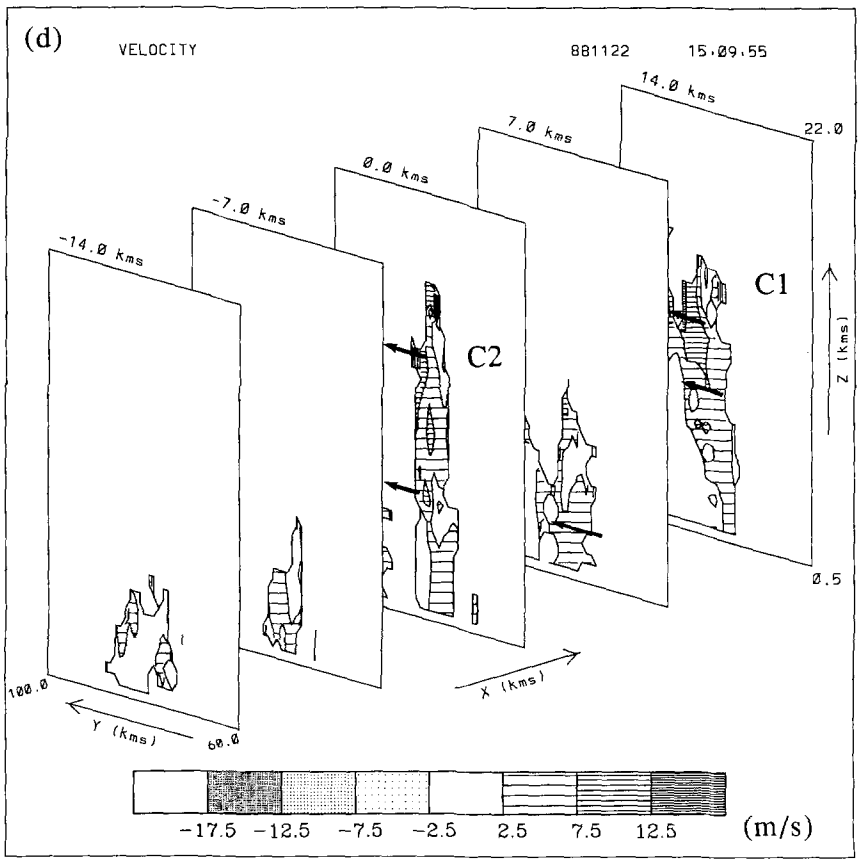

Fig. 12. (*Continued*)

($T = -15\,°C$) in the region where liquid water can still exist (see Section 5). Towers associated with C1 and C2 have much weaker echoes (maximum 34 dBZ_e) and are likely composed entirely of ice. The Doppler data show strong radial motion away from the radar throughout most of the complex with maximum velocities above 8 km height. An anvil is apparent between 8–14 km height at the eastern edge of the complex and the western edge of the merged system is shallow, not extending above 6 km height.

The north-south cross-sections at 1509 CST shown in Figs. 12c–d indicate there is a weak echo region (WER) at 11 km height within C2. Associated with the WER is a maximum in the front-to-rear flow sloped $\sim 70°$ from the horizontal i.e. quite erect. Assuming environmental conditions for the horizontal wind components (u, v), the vertical motion (w) can be estimated from the relation:

$$V_r = u\cos\phi\sin\theta + v\cos\phi\cos\theta + (w + V_t)\sin\phi, \quad (1)$$

where V_r is the Doppler measured radial velocity, V_t is the particle fall speed estimated from the empirical radar reflectivity relationship given by Atlas et al. (1973), and ϕ, θ represent the antenna azimuth and elevation, respectively. Although error prone, the vertical velocity estimate from (1) ranged from 25–60 $m\,s^{-1}$, which overlaps with that obtained previously using the echo-top rise rate.

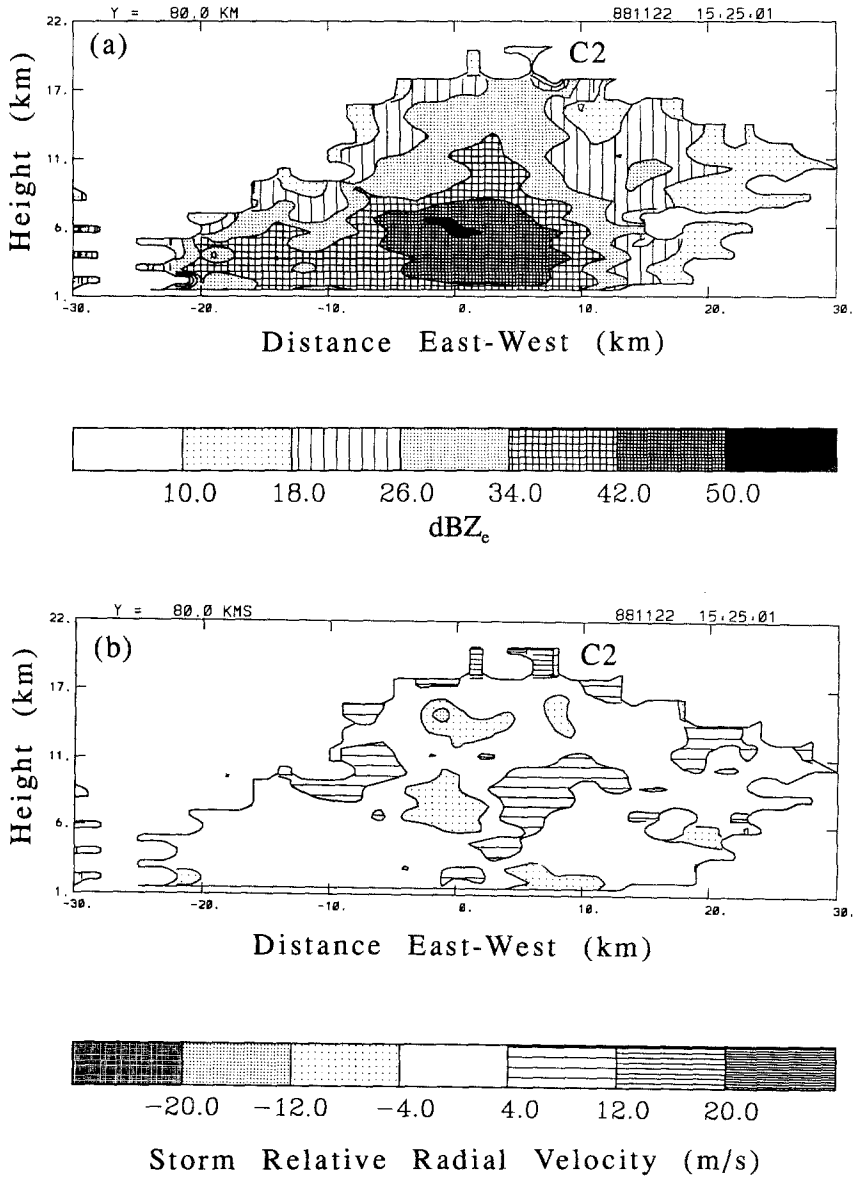

Fig. 13. Vertical cross-sections through island thunderstorm at 1525 CST. See Fig. 11 for details and Fig. 10c for location of cross-sections. In (c) arrows denote location of constriction and weak echo region (WER). Storm motion is from 0° at 1.7 $m\,s^{-1}$. Note small area of reflectivity greater than 50 dBZ_e near $z = 5$ km and $x = 0$ km

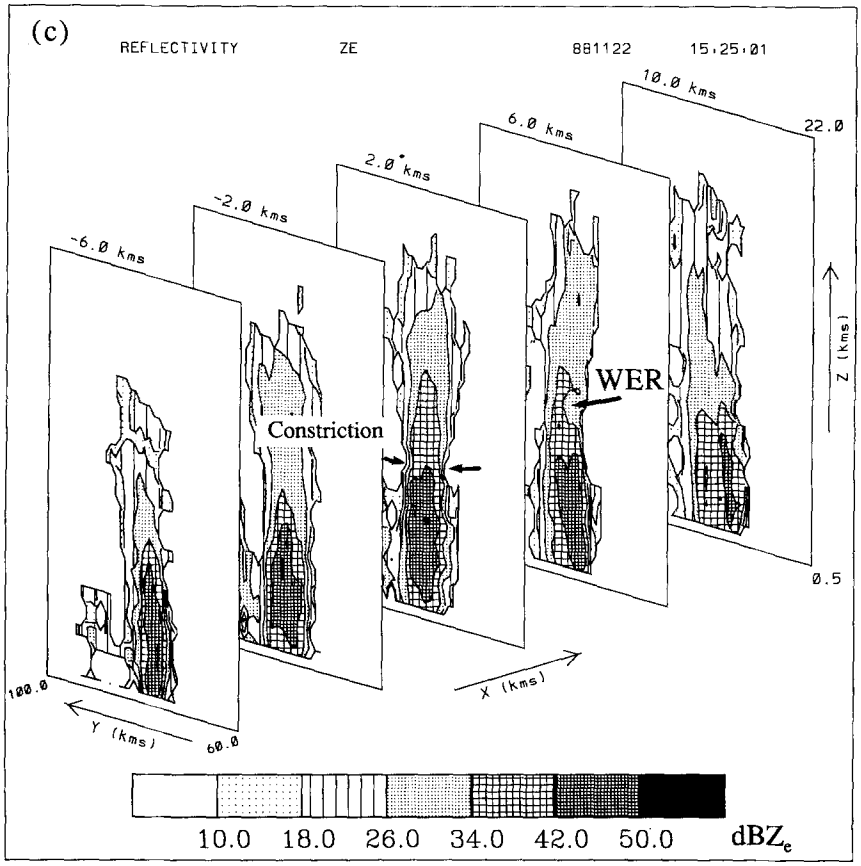

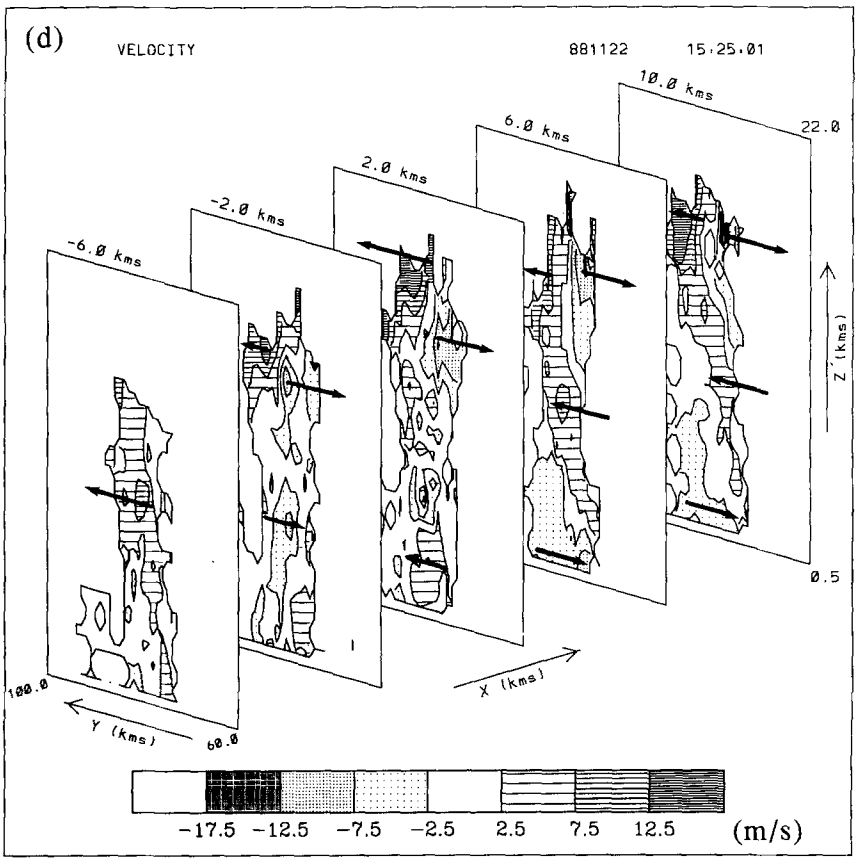

Fig. 13. (*Continued*)

There is evidence in Fig. 12 for discontinuous updraught structure near 6 km for C2 and a reflectivity constriction of the type described by Kingsmill and Wakimoto (1991). This may be evidence for a rapid increase in updraught intensity with height resulting from the large amount of CAPE in the mid-to-upper environment (see Fig. 2) as well as precipitation unloading above the melting level within the updraughts as will be discussed in Section 5. Front-to-rear flow being expelled behind the system (northwards) is evident at the top of C1 and C2.

Cell C1 at this time has started to develop a forward overhanging anvil at heights from 12–13 km. In this cell, the front-to-rear flow is more continuous than in C2 and slopes more in the horizontal ($\sim 40°$). Up to this stage there is no evidence of significant storm-relative rear-to-front flow. The complex is moving at approximately the speed of the flow on the northern side of the storm.

4.3.3 Reorientation Stage

At 1525 CST (Fig. 10c) the entire mesoscale system is merged at the 42–50 dBZ_e level and has the appearance of an inverted V. It is reorienting, starting to lose the west-to-east alignment evident at 1509 CST and is developing toward a more northwest to southeast alignment. This organisation was manifested as:

1. The northern flank of L1 dissipated with the southern flank of L1 continuing to move westward south of C2,
2. Continued westward motion of the northern flank of L2.

Along the east-west direction at $y = 80$ km, through the apex of the inverted V as shown in Figs. 13a–b, it is evident that C2 is at least 20 km deep. Echoes up to 26–34 dBZ_e intensity detected to heights of 18 km with maximum echo strength greater than 50 dBZ_e detected near the melting level at 5 km. An extensive anvil echo has developed on the eastern edge and extends from heights of 7 km to near 16 km.

The strongest and deepest reflectivities above 6 km are located between the motion radially away and radially towards the radar. The weaker reflectivities to the west ($x < 0$ km) have radial motion towards the radar between 6 km and 10 km. There is notching and an associated downsloping reflectivity minimum associated with this middle-level rear-to-front flow. The radial motion towards the radar evident above 13 km in Fig. 13 is interpreted as rear-to-front anvil outflow. Maximum reflectivities are located at 5–6 km height in the region of the mid-level rear-to-front flow.

At 8 km height, there is evidence in Fig. 14a–b for adjacent anticyclonic and cyclonic vortices embedded within the storm at 1525 CST. The midpoint between the two 5 km wide vortices was located near the apex of the inverted V structure. The vortices were first apparent at 1518 CST at a height of 8 km and were still detectable at 1530 CST.

The vertical structure of the storm viewed in north-south sections at 1525 CST indicates differences on both flanks as shown in Fig. 13c–d. On both the eastern and western flanks, where the storm has a more north-west to south-east oriented structure, the Doppler motion indicates a continuous and highly slanted (45° from horizontal) front-to-rear flow or updraught. This slant is evident in the reflectivity fields at $x = 6$ and $x = 10$ km in Fig. 13c. At $x = 6$ km, there is evidence for a WER in the 34–42 dBZ_e reflectivity structure near 8 km.

In the centre of the storm ($x = -2$ and 2 km), front-to-rear flow is not as continuous. The middle level rear-to-front flow evident from 6–10 km height on the western side of the storm also breaks the continuity of the updraught. At $x = 2$ km, the constriction or horizontal notching near 8 km height is still evident. The location of the constriction coincides with the separation in the front-to-rear updraught just above the melting level.

On the eastern edge of the storm ($x = 6$ km in Fig. 13d), there is storm relative rear-to-front flow in the PBL at the leading edge of the storm. Cold pool production, presumably by evaporation and melting underneath the precipitation maximum in the region of the slanted updraughts, and a descending channel of rear-to-front flow starting at heights near 3–4 km is seen at $x = 6$ km and $x = 10$ km. In the region where the orientation of the storm is changing rapidly, there is evidence for slanted, deep, and well-developed updraughts, with cold pool production in the PBL.

At upper levels (15–17 km height), the Doppler structure shows diffluent outflow, consisting of a front-to-rear and rear-to-front couplet located above the precipitation maxima.

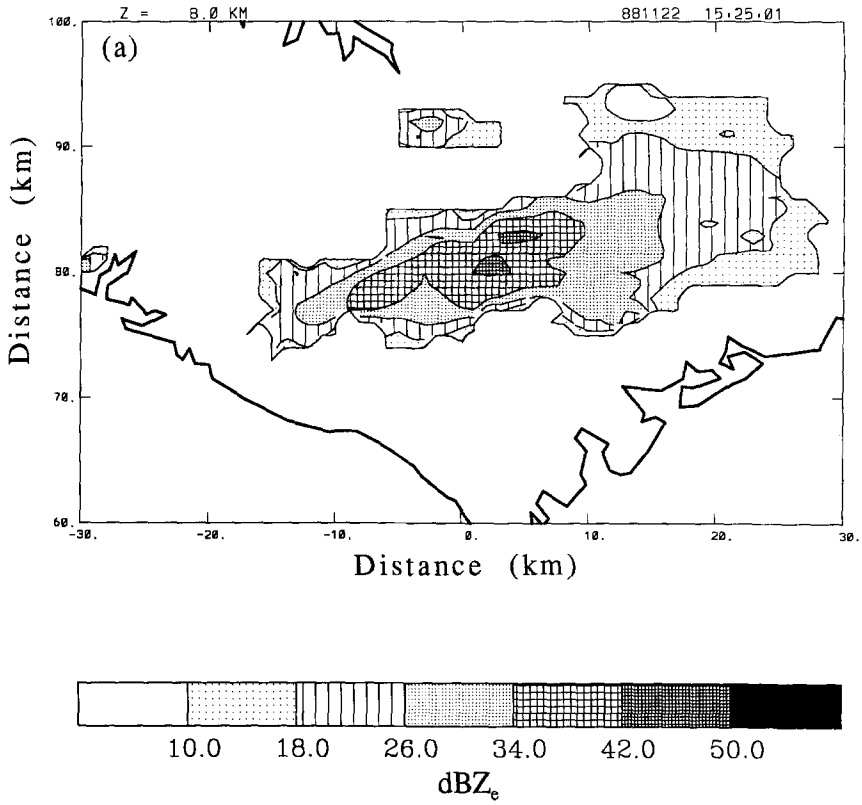

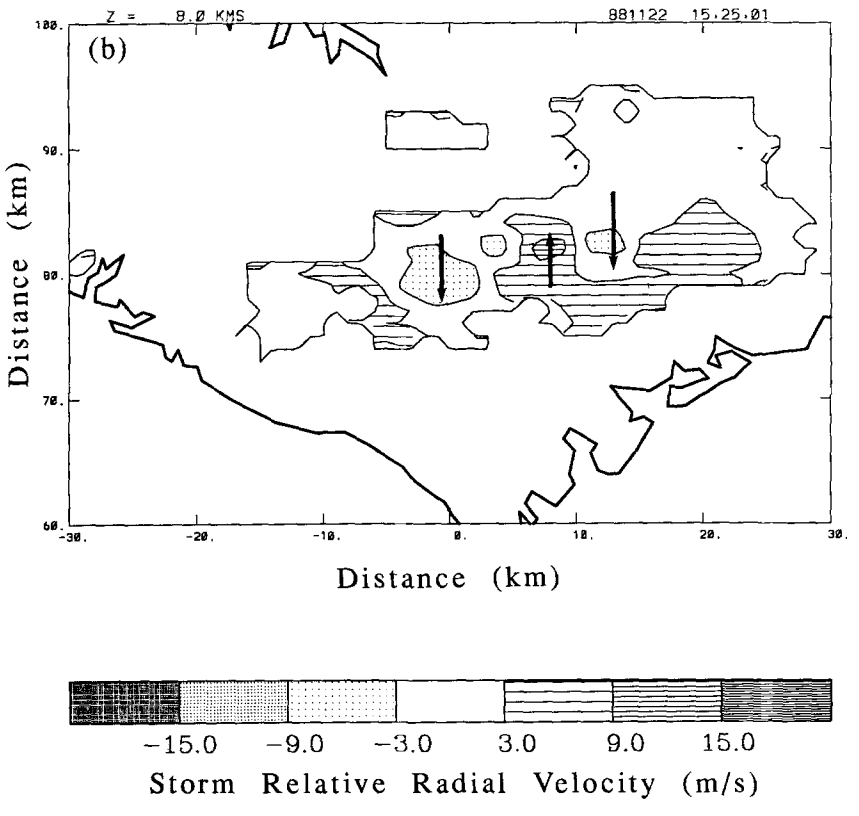

Fig. 14. CAPPI through island thunderstorm on 22 November 1988 at 1525 CST. (a) Reflectivity field (dBZ_e) at 8 km height, (b) Doppler derived storm relative radial velocity field ($m\,s^{-1}$) at 8 km. Storm motion is from 0° at $1.7\,m\,s^{-1}$. Arrows indicate sense of storm relative flow

In the time-height section of Fig. 8, maximum echo top was approximately 20 km at 1525 CST. This is at least 2–3 km higher than the tropopause height, which was between 17 and 18 km based on the GP 1030 CST sounding. Neglecting nonhydrostatic pressure gradient forces, Malkus (1960) estimated that a vertical velocity of about 20 m s^{-1} is required for every 1 km of penetration into the stratosphere based on typical lower stratospheric stability and parcel theory[7]. This would imply 40–60 m s^{-1} peak vertical velocities within the storm.

4.4 Mature Multicellular Squall Stage

By 1540 CST, the system is organised in the fashion of a multicellular squall line with the leading convective cells aligned in the north-west to south-east band (L3 in Figs. 6e and 10d) and a stratiform band trailing behind to the north-east. The east-west cross-section through the remains of C2 in Figs. 15a–b indicates a much weaker storm than observed at 1525 CST, although echo tops are still in excess of 18 km high.

The north-south cross sections through the storm in Fig. 15c–d show the multicellular nature of the storm. Evident along $x = 0$ km is highly slanted (30° from the horizontal) front-to-rear flow overlying rear-to-front PBL flow. Maximum velocities within this front-to-rear flow are again at 6–10 km height and above the maximum precipitation echo. A new intense cell is forming over the rear-to-front flow of the cold pool and a more mature cell is evident 10 km to the rear. Maximum outflow is concentrated above the mature cell near the tropopause level ($\sim$16 km). It is interesting to note that radar-observed velocities in the cold pool are up to 12 m s^{-1} faster than the speed of the storm. A trailing anvil is evident behind the storm. The internal draught structure is less clear on the weaker peripheral zones of the storm. This latter structure of the storm is very similar to the classic squall line structures discussed by Rotunno et al. (1988) and Rutledge (1991).

[7] This relationship was given support by experiments on laboratory thermals in a tank of stratified liquid (Simpson, 1983).

5. Model Simulations, Cloud Microphysics and Dynamics of the Thunderstorm

In the Simpson et al. (1993) study, the one-dimensional, time-dependent (1DTD) cloud model of Ferrier and Houze (1989) estimated the heights and updraught strengths of a Hector in the November 22, 1988 environment (Fig. 2a) using reasonable initial forcing based on previous cumulus studies. The cloud-top heights of Hector were well simulated, as was the general strength and configuration of the radar echo. The peak model updraught was nearly 40 m s^{-1} at the 16 km level. A modified Lin et al. (1983) three-class ice scheme was used. The intercept in the particle size distribution assumed for hail was increased by three orders of magnitude in order to reflect the particle size distribution for frozen drops characteristic of tropical convection rather than the larger ice particles parameterised in Lin et al. (1983) for midlatitude hailstorms.

The same 1DTD model is used in this study, but with a new four-class ice formulation of Ferrier[8] (1993) that calculates the mixing ratios of *cloud ice*, low density *snow*, moderate density *graupel* (Rutledge and Hobbs, 1984), and high density *frozen drops* (Simpson et al., 1993). The size distributions of snow and graupel parameterised in the model are similar to those assumed in Rutledge and Hobbs (1984), whereas the higher concentrations of frozen drops[9] are parameterized for the following reasons: (1) to simulate maximum radar reflectivities in the model that are consistent with the radar-observed peak reflectivities of 50–55 dBZ, and (2) to match closely the assumed intercept of the raindrop distribution of 2.2×10^7 m^{-4} for tropical rainfall (Lord et al., 1984), given that copious amounts of rain freeze to form these large ice particles (Simpson et al., 1993).

The control simulation and eighteen sensitivity experiments are described in Table 3, and their results are summarised in Table 4. The input environment used in all of the model runs is the 1330 CST sounding from GP (Fig. 2). The con-

[8] This version of the Ferrier (1993) scheme does not calculate ice-particle concentrations and liquid water mixing ratios on ice.

[9] Intercepts of 5×10^6 m^{-4} are assumed for the snow and graupel distributions and 2.2×10^7 m^{-4} for the size spectra of frozen drops.

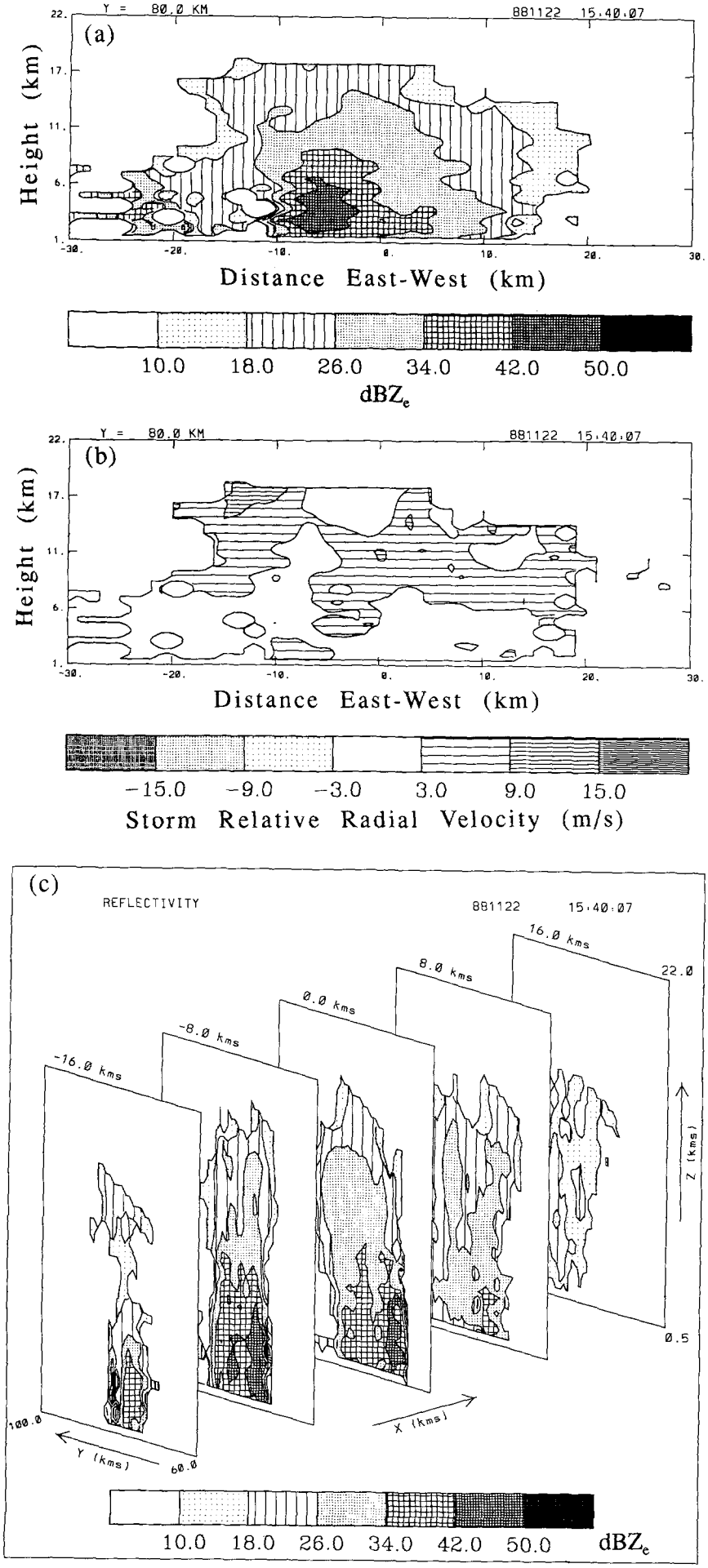

Fig. 15. Vertical cross-sections through island thunderstorm at 1540 CST. See Fig. 11 for details and Fig. 10d for location of cross-sections. Storm motion is from 72° at 5.2 m s^{-1}. In (d), arrows indicate sense of storm relative flow

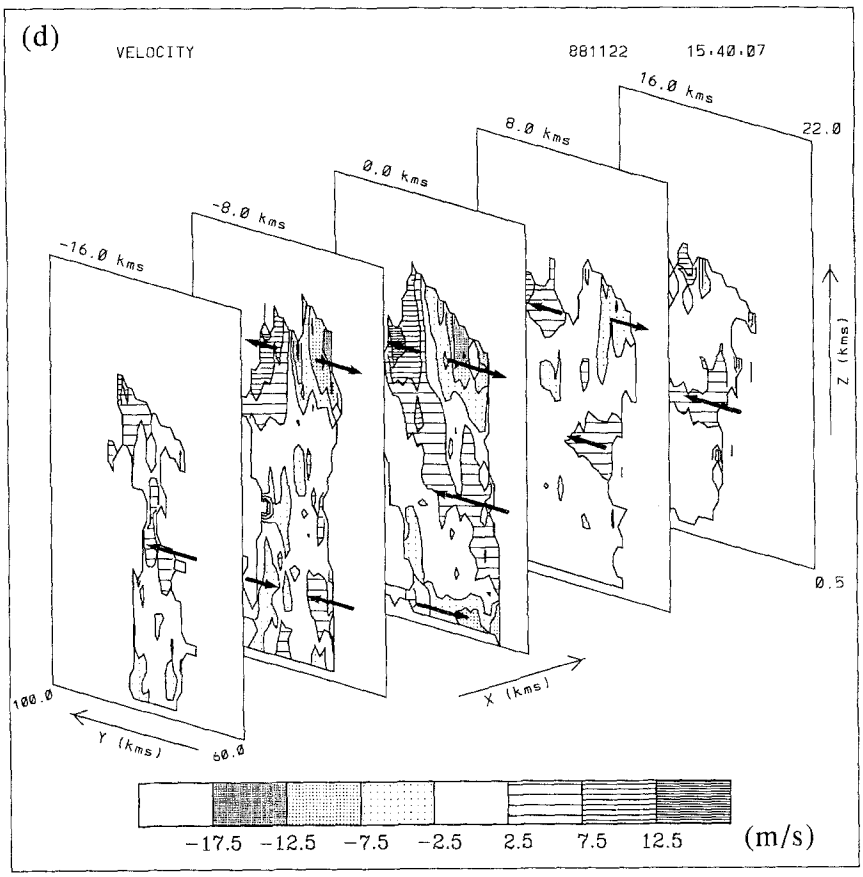

Fig. 15. (*Continued*)

vection was initiated as described in Simpson et al. (1993) by gradually imposing a peak updraught of 2.0 m s^{-1} at 600 m during the first ten minutes of each run.

5.1 Control Simulation

The control simulation is shown in Fig. 16 (run A in Table 3). The features of this model cloud differ little from that with the less sophisticated ice microphysics used in Simpson et al. (1993) due to the dominance of frozen drops in the convection. In fact, maximum mixing ratios of frozen drops are an order of magnitude larger than the maximum mixing ratios of snow and graupel. The cloud-top temperature for the control run in Fig. 16 is $-92\,^{\circ}$C, nearly as cold as the observed tops in Tropical Cyclone Hilda (Ebert and Holland, 1992). The simulated updraught is about 30 m s^{-1} at the tropopause, lower than the 38 m s^{-1} estimated for the above tropical cyclone, but consistent with estimates based on the echo-top rise rates (Fig. 8), Doppler-derived radial motions (Fig. 12), depth of cloud penetration into the stratosphere, and mesoscale model simulations (Golding, 1993).

The updraught speeds are comparable in their intensity to those observed in severe supercell storms (Miller et al., 1988; Bluestein et al., 1988), and their location at upper levels is consistent with the suspected presence of a WER above 8 km. Although such features are traditionally associated with supercell storms, they have also been observed in multicellular storms (Chisholm, 1973). Furthermore, rapid increases in vertical velocity with height (i.e., $dw/dz > 0$) produce strong horizontal convergence into the updraught, which is hypothesised to have resulted in the formation of a reflectivity constriction near 8 km (Figs. 12c and 13c; see Kingsmill and Wakimoto, 1991). A peak horizontal convergence of $-7 \times 10^{-3}\,s^{-1}$ developed at the 10 km level in the control run, where updraught speeds increased rapidly with height primarily in response to a deep layer of environmental instability between 400 mb and 100 mb, and aided to a lesser extent by substantial precipitation loading below 7 km.

The cloud base simulated in the control run was 1.3 km. The height of the first radar echo, defined by a reflectivity threshold of 20 dBZ, was at 3.9 km, which is close to the maximum height

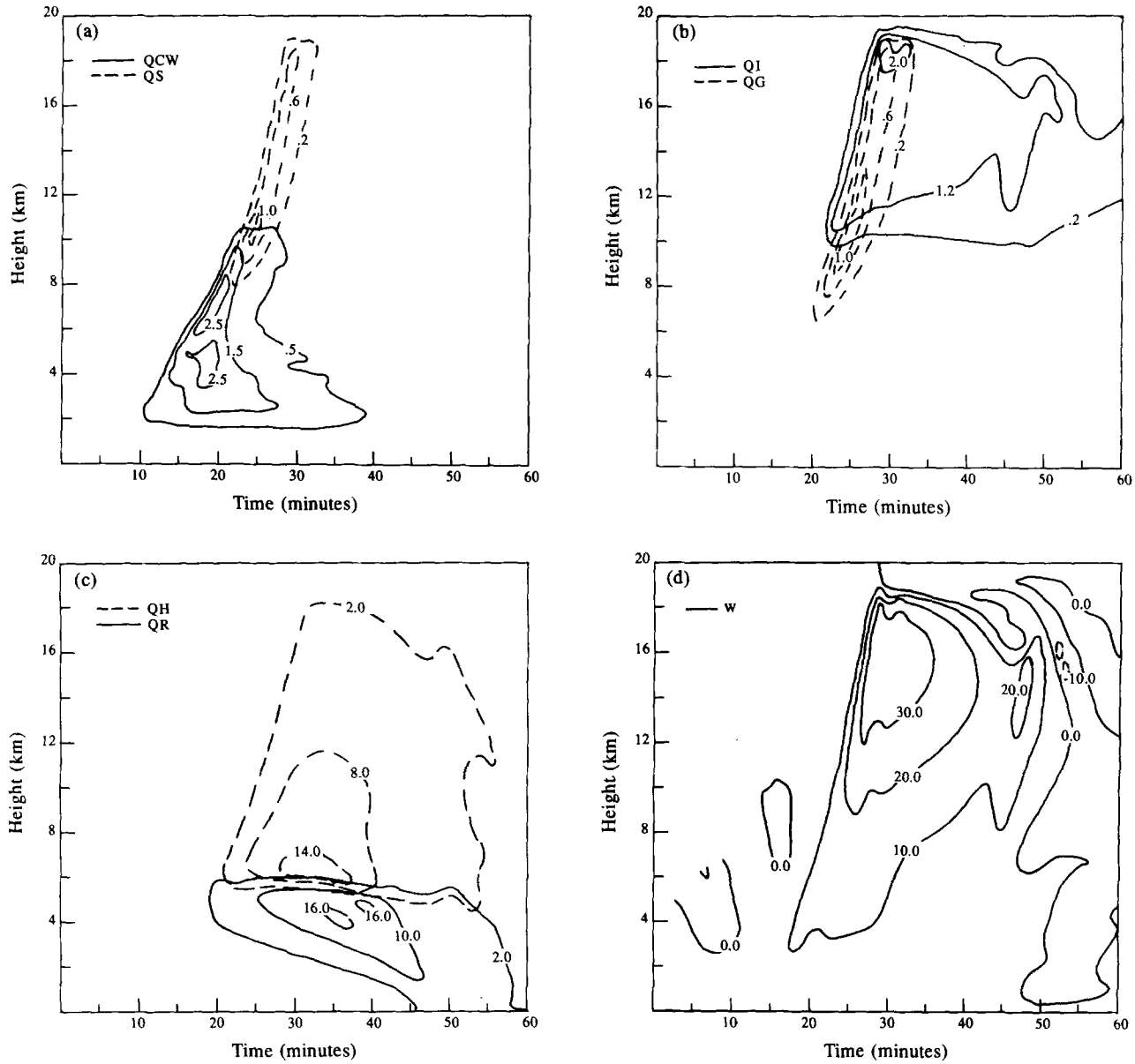

Fig. 16. Time-height sections from the control simulation (run A) using the one-dimensional cloud model of (a) cloud water (QCW) and snow (QS), (b) cloud ice (QI) and graupel (QG), (c) hail (QH) and rain (QR) and (d) vertical velocity ($m\,s^{-1}$). Hydrometeor fields unit are $g\,kg^{-1}$

observed in GATE (see Fig. 14 of Szoke et al., 1986). The first echoes formed from warm rain processes in the presence of mean updraught speeds of $\sim 5.5\,m\,s^{-1}$ between 2 and 4 km. At the time of onset of the initial echoes at 10 min into the simulation, the convection was able to penetrate through the stable layer despite temperature deficts of $-1.4\,°C$ at 2.9 km. The model simulates well the height of initial precipitation shown on the radar. Elevated radar first echoes above the melting level, indicative of precipitation initiation from ice-phase processes, were not observed at any time during the study. Therefore, the simulations and radar observations both suggest that precipitation was initiated through warm-rain mechanisms.

Ice was initiated at 7.1 km by 19 min into the control run. Explosive vertical development associated with these thunderstorms is already underway by this time as the cloud grew to 7.7 km, peak updraughts reached $12.1\,m\,s^{-1}$ at the 3.6 km level, and a maximum radar reflectivity of 40 dBZ had formed at 4.5 km (in association with rain water contents of $1.28\,g\,m^{-3}$). Supercooled rain-

Table 3. *Descriptions of each of the Model Runs Discussed in the Text, such as the Sensitivity of the Convection to Changes in the Ice-Phase (runs B1–B6) and Warm Rain (runs C1–C2) Microphysics, Increasing the Tropopause Temperature (runs D1–D3), Lowering the Surface Temperature (runs E1–E4), Increased Dynamic Entrainment (run F), and Precipitation Unloading from Slanted Updraughts* (runs G1–G2). The latent heats of vaporisation, sublimation and fusion are represented symbolically by L_v, L_s and L_f respecitively

Run	Description
A	Control Simulation: 4 ice classes, Fig. 16
B1	No latent heating of fusion (freezing still converts water to ice, but no diabatic heating is allowed by setting $L_f = 0$.
B2	Same as B1, but heating by deposition is made the same as condensation (i.e. $L_f = 0$ and $L_s = L_v$)
B3	Same as B2, except deposition rates adjust to water rather than ice saturation.
B4	No ice (cloud and rain only)
B5	Delayed initiation of ice crystals until $T < -20\,°C$
B6	Ice Multiplication (10^3 more cloud ice particles-concentration of $1\,L^{-1}$ at the 0 °C level rather than $10^{-5}\,L^{-1}$ in control run)
C1	Cloud water autoconversion threshold to rain = $0.2\,g\,kg^{-1}$ ($1.0\,g\,kg^{-1}$ in control run) corresponds to $n_w \sim 50\,cm^{-3}$
C2	Cloud water autoconversion threshold to rain = $2.0\,g\,kg^{-1}$ ($n_w \sim 500\,cm^{-3}$)
D1	Minimum sounding temperature of $T_{min} = -80\,°C$ (>1 °C warming at 16.2–19.0 km; minimum sounding temperature was −88 °C)
D2	$T_{min} = -70\,°C$ (>1 °C warming at 14.8–19.2 km)
D3	$T_{min} = -60\,°C$ (>1 °C warming at 13.4–21.2 km)
E1	$T_{sfc} = 32.0\,°C$ (screen temperature of sounding was 32.2 °C)
E2	$T_{sfc} = 31.5\,°C$
E3	$T_{sfc} = 31.0\,°C$
E4	$T_{sfc} = 30.9\,°C$ (well-mixed boundary layer)
F	Constant cell radius (increased dynamic entrainment)
G1	Updraught tilted 20° from vertical axis
G2	Updraught tilted 60° from vertical axis

drops present up to 7 km froze very rapidly to form predominately frozen drops, consistent with dual-polarised radar observations of developing continental convection (Illingworth et al., 1987; Wakimoto and Bringi, 1988; Tuttle et al., 1989). Aircraft observations of graupel in developing cumuli over Florida suggest that rime splintering may have also been effective in promoting secondary ice production in island thunderstorms (Hallett et al., 1978). Although rime-splintering is not represented in this simpler version of the four-class ice scheme, the coexistence of large concentrations of graupel and frozen drops with cloud water (i.e., QCW and QG fields) in Fig. 16 indicates that rapid secondary ice production is possible after 22 min in the 6–7 km layer, where rime-splintering is believed to be active in the presence of updraught temperatures between −2 °C and −8 °C (Hallett and Mossop, 1974; Mossop, 1985). Yet, the island thunderstorm has already reached its mature stage of development by this time.

5.2 *Microphysical Sensitivity Experiments (runs B1–B6, C1–C2)*

The sensitivity of the modelled convection to diminished effects of the ice phase are considered in runs B1–B5, whereas run B6 simulates the increased influence of fusion by means of "ice-amplification". The largest effects of reduced ice are manifested in smaller updraught velocities, while simulated ice multiplication increases slightly the peak updraught. Yet, the net condensation and deposition (i.e., condensation and deposition minus evaporation and sublimation) integrated throughout the lifetime of the cell (C_{net}), which is a useful indicator of the overall intensity of the convection, changes very little in association with differences in the treatment of the ice phase. This is because much of the heating occurs at lower levels where the water vapour mixing ratios are large. Following the thermodynamic energy equation,

$$\frac{d\theta}{dt} = L_v/(\pi C_p)QCND, \tag{2}$$

where θ is the potential temperature, L_v is the latent heat of condensation, π is the Exner function $(p/p_0)^{0.285}$, $C_p = 1005.7\,J\,kg^{-1}\,K^{-1}$ and QCND is the condensation rate, the in-cloud potential temperature (and therefore cloud buoyancy) will increase with height for the same rate of condensation due to π decreasing with height. Since the maximum updraught speeds are located near 15 km height, small changes in diabatic heating in the clouds will result in a large dynamic response at upper levels. The effects of the ice phase upon the cloud top height are small, given that peak clouds top heights vary by less than 1 km between runs A and B1–B6.

Maximum potential temperature perturbations in the updraught of run A reached at 8.4 °C at 11.7 km. Altough the updraught temperatures in run A were more than one degree warmer than in runs B1–B4 only above 8 km, the effects of the ice phase upon cloud buoyancy were greatest between 12.5 km and 13.5 km where the updraught in run A was 3–4 degrees warmer than in runs B1–B4. Delaying the onset of ice in run B5 had little impact upon the convection. The effects of ice multiplication were crudely represented in run B6 by increasing the cloud-ice number concentrations by 5 orders of magnitude with respect to the control run (see Lin et al., 1983 for description of cloud ice nuclei concentrations following Fletcher, 1962). The result of this "ice multiplication" was greatest in rapidly removing supercooled cloud water. Homogeneous freezing of cloud drops (−40 °C) near 11 km occurred in run A, whereas cloud water did not extend above the 8 km level (near −20 °C) in run B6. The updraught in B6 was only a little more than 0.5 °C warmer than the control run between 8.5 and 10 km, thus accounting for the similarity in updraught strengths in the simulations. The high (>8.5 °C) potential temperature perturbations (not shown) in runs A and B1–B6 are a result of subsidence warming above 17 km in response to the strong overshooting cloud tops.

Given that updraughts speeds through the freezing level already exceed 10 m s^{-1} in runs A and B1–B6, the additional heating by ice is of secondary importance in explaining the overall intensity of the thunderstorm. The similarity in the time-height cross sections between these runs (not shown), as well as results from Table 4, imply that it would be difficult to observe the impact of ice processes upon convective cells in island thunderstorms[10]. An important result is that the crude representation of the ice phase used in the mesoscale model of these storms undertaken by Golding (1993) should not significantly degrade the realism of the dynamical results Golding's simulations produced 30 m s^{-1} vertical velocities at 10–15 km height and larger peak values at higher levels, including a 60 m s^{-1} updraught in a merger over Aspley Strait.

The impact of continental versus maritime air masses upon the simulated convection is crudely assessed in runs C1–C2 by noting that autoconversion of cloud water to rain often occurs when the mean cloud droplet diameter reaches 20 μm (Manton and Cotton, 1977; Cotton et al., 1982; Banta and Hanson, 1987). Although more accurate evaluation requires the use of an explicit warm rain scheme (e.g., Clark, 1973; Soong, 1974; Kogan, 1991), our experience with bulk parameterisations indicates that simulated convection is much more sensitive to changes in the threshold cloud water mixing ratio (q_{wo}) than the autoconversion rate. A pristine maritime environment is assumed in run C1, where $q_{wo} = 0.2\,\mathrm{g\,kg^{-1}}$ is appropriate for a droplet number concentration (n_w) of $\approx 50\,\mathrm{cm^{-3}}$ at an air density of $1\,\mathrm{kg\,m^{-3}}$. A value of $q_{wo} = 2.0\,\mathrm{g\,kg^{-1}}$ in run C2 is typical of continental conditions where $n_w \approx 500\,\mathrm{cm^{-3}}$. Table 4 shows that the simulated convection is only slightly more intense in run C2 when the formation of rain is delayed. But, as expected, Table 5 indicates that the greater effect of droplet number concentration is on the initiation of precipitation, which can be delayed significantly in continental versus maritime air masses. Precipitation was initiated by warm rain processes in all of the runs. Even though the freezing level is at 5.1 km, no ice was present in run C2 when 20 dBZ radar echoes first formed at 4.9 km.

5.3 Environmental (runs D1–E4) and Dynamical (runs F-G2) Sensitivity Experiments

Given the very cold temperature (∼ −80 °C) of the tropopause, the effects of the tropopause height upon the thunderstorms are evaluated in simulations D1–D3. As expected, the greatest impact in varying the tropopause is upon the simulated cloud-top heights. However, noticeable effects upon the peak updraught speeds only occur when the tropopause is lowered to 13.4 km.

Surface temperature changes had by far the greatest impact upon the simulations of the thunderstorms, as shown in runs E1–E4. Gradual cooling near the surface dramatically reduced the thunderstorm intensity, such that when the surface temperature was cooled to 30.9 °C in E4 in order to produce a well mixed surface layer, only fair-

[10] The presence versus the absence of ice processes can make very large differences in cloud dynamics in other environments, for example, under some conditions in Florida and the Caribbean.

Table 4. *Summary of the Results of each of the Experiments Described in Table 3.* Maximum values are shown of the cloud-top height (Z_t in km, which is defined by a hydrometeor mixing ratio of 0.1 g kg^{-1}), updraught velocity (w_{max} in m s^{-1}), potential temperature deviation from the large-scale environment (θ_{max} in deg C), total hydrometeor content (q_{max} in g kg^{-1}), surface rain rate (RR_{max} mm h^{-1}). Minimum values are listed for downdraught speed (w_{min} in m s^{-1}), perturbation potential temperature (θ_{min} in deg C), as well as downdraught velocity (W_d in m s^{-1}) and perturbation potential temperature (θ_d in deg C) below the melting level. The net condensation and deposition in the 1 hour simulations is given by C_{net} (10^9 kg)

Run	Z_t	w_{max}	θ_{max}	q_{max}	RR_{max}	w_{min}	θ_{min}	w_d	θ_d	C_{net}
A	19.7	38.8	10.9	21.0	125.7	−12.3	−55.2	−4.6	−3.4	1.2
B1	19.2	32.0	10.0	21.8	119.2	−10.7	−35.0	−5.0	−3.4	1.2
B2	19.1	29.3	10.2	21.9	135.4	−12.4	−39.6	−5.1	−3.4	1.2
B3	19.0	28.6	8.6	21.8	147.6	−10.6	−31.0	−5.1	−3.4	1.2
B4	19.0	28.6	10.0	18.2	111.2	−10.5	−32.9	−3.5	−3.4	1.2
B5	19.7	38.6	10.6	21.0	120.8	−12.2	−55.1	−4.6	−3.4	1.2
B6	19.9	39.7	10.4	20.7	134.9	−12.6	−55.1	−4.9	−3.4	1.3
C1	19.7	38.5	10.8	19.9	137.2	−12.5	−54.3	−5.2	−3.3	1.1
C2	19.8	39.4	13.0	22.5	98.5	−13.3	−59.7	−4.9	−3.4	1.5
D1	19.2	38.9	8.4	21.0	125.8	−11.8	−46.7	−4.6	−3.4	1.2
D2	18.1	37.9	8.4	21.0	126.8	−12.0	−42.5	−4.6	−3.4	1.2
D3	17.4	32.7	8.5	21.0	114.2	−10.5	−51.7	−4.6	−3.4	1.2
E1	19.6	37.2	9.8	18.6	126.8	−12.9	−53.7	−4.8	−3.2	0.97
E2	18.4	26.2	7.4	11.9	86.7	−8.8	−17.1	−4.1	−3.7	0.56
E3	10.4	9.8	2.4	5.9	42.5	−2.9	−4.3	−2.9	−3.4	0.37
E4	2.6	2.9	1.1	0.3	0.0	−2.5	−2.4	−2.5	−2.4	0.005
F	16.5	19.1	3.7	11.7	147.2	−7.3	−6.8	−4.6	−3.5	0.9
G1	20.2	41.5	10.5	11.6	27.7	−13.0	−67.2	−0.3	−3.4	2.3
G2	20.5	44.4	9.2	8.2	0.0	−10.9	−75.2	−0.3	−3.4	2.6

Table 5. *Sensitivity of the Height (Z_{r1}) and Time (T_{r1}) that Drops Initially form, as well as the Height (Z_{r1}) and Time (T_{r1}) that 20 dBZ Radar Echoes First Develop, are Tested as Functions of Droplet Number Concentration (n_w) and Updraught Strength.* The effects of n_w upon the threshold cloud water mixing ratio for autoconversion to rain (q_{wo}) are considered in runs A and C1–C2. The effects of surface temperature (T_{sfc}) upon updraught intensity are considered in runs *A* and E1–E3 (see Tables 3 and 4). The 20 dBZ threshold was selected to compare with the radar statistics of GATE cells compiled by Szoke et al. (1986) and Szoke and Zipser (1986)

Run	n_w (cm^{-3})/q_{wo} (g kg^{-1})	T_{sfc}	Initial drop formation		First 20 dBZ echo	
			Z_{r1} (km)	T_{r1} (min)	Z_{r1} (km)	T_{ri} (min)
A	239/1.0	32.2	2.3	12.1	3.9	15.2
C1	48/0.2	32.2	2.1	8.7	2.3	12.7
C2	477/2.0	32.2	4.5	15.0	4.9	17.3
E1	239/1.0	32.0	2.3	12.7	3.7	15.9
E2	239/1.0	31.5	2.3	16.4	2.7	19.8
E3	239/1.0	31.0	2.7	21.2	2.7	35.3

weather cumuli were produced with no surface precipitation. Table 5 shows that the updraught intensity at lower levels can significantly raise the height of the 20 dBZ radar first echo, while having little impact on the height that rain is initiated in the clouds. The effects of increased dynamic entrainment, which is represented by assuming a constant updraught radius is run *F*, were also significant in reducing the thunderstorm intensity. The fall of precipitation out of tilted updraughts in runs G1–G2 prevented the development of low-level downdraughts, resulting in quasi-steady

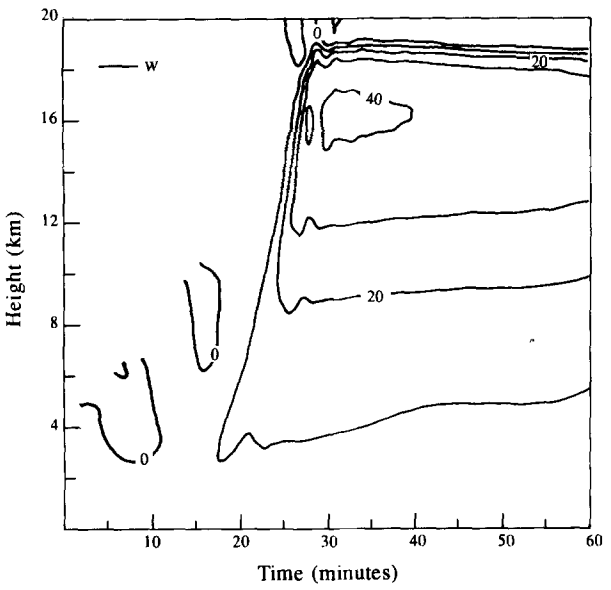

Fig. 17. Time-height section of vertical velocity ($m\,s^{-1}$) for run (G1) with updraught tilted 20° from vertical axis

convection after 30–35 min into the simulations (Fig. 17) and nearly a factor of two increase in net condensation over the control run (Table 4). Clearly, these environmental and dynamical factors are more much important in affecting the nature of the thunderstorm than the effects of ice.

A very important environmental factor affecting the development of deep thunderstorms is the presence of a dry, stable layer at 2.3–2.9 km. This layer is beilieved to be a result of subsidence, since the relative humidity decreases from 83 to 46 percent from the bottom to the top of the layer. The excess potential temperature in the most intense stage of the updraught core in run A is less than 0.1 °C at 2.9 km. Consequently, this layer can act as an effective lid to weaker convective cores, and it was of critical importance in preventing the development of deep convection in runs E3 and E4. Although Table 5 shows that rain in the control run was initiated at 2.3 km, the first formation of the 20 dBZ echo was delayed until 3.9 km, after the updraught had penetrated through the stable layer.

These model results give facinating suggestions regarding diurnal changes in the forcing mechanisms that produce, maintain and reorientate these island thunderstorms. The effectiveness of a warm surface temperature, and implied importance of fluxes of heat and moisture from the surface in raising the equivalent potential temperature (θ_e) of the lower boundary layer, indicate that little dynamical forcing by updraughts at cloud base are needed by midafternoon. Earlier in the day, it appears that strong dynamical forcing by sea-breeze convergence may be necessary for penetrative convection to occur when the CAPE is substantially less (Table 2). As precipitation and its associated gust-front outflows become active, a new forcing mechanism for convective growth and propagation comes into play, which was described as "mining the boundary layer" in Simpson et al. (1993). Cool downdraughts are hypothesised to be the mechanism of reorientation and westward propagation of the system. They instigate new convective growth in the high energy boundary layer to the west and kill convection by bringing down low θ_e air to the east, thereby drying and stabilising the boundary layer there.

Further progress in simulating and understanding the evolution of convective forcing during the day requires a three-dimensional model, aided by more detailed observations of the lower boundary layer and of the evolving clouds over the island.

6. Discussion

6.1 Merger and Reorientation Process

In this case, mergers resulted in the development of separate mesoscale systems over both islands, and eventually one mesoscale system formed from merging of these systems. Over Bathurst Island, initial cells (see Figs. 6a–b) merged by 1508 CST into an east-west line in the region of sea breeze convergence shown in Fig. 3c. Over Melville island, C2 grew to be the dominant cell with rapid vertical growth and intense vertical velocities within the line L2. Bridging and merging was observed within the cells forming L2 and between L2 and L1 in the formation of this Melville Island complex. By 1543 CST, as shown in Fig. 6c and Fig. 7, the complexes over both islands had merged into one essentially east-west aligned complex. This complex gradually re-oriented to a north-south direction by 1700 CST (L3 in Fig. 6e) and moved off to the west.

Observational studies confirm the importance of pre-existing low-level convergence (Simpson et al., 1980) in promoting mergers. This is supported

by the modelling study of Tao and Simpson (1989). The data presented herein validates this concept as the major mergers occurred in a pre-existing region of low-level convergence, as indicated by the sea breeze simulations presented in Fig. 3. In addition, all major complexes evident before the island to island merger (L1, L2, and the Bathurst Island complex evident in Fig. 6c at 1533 CST) were capable of merger by gust fronts spreading westward, which is consistent with the easterly flow at mid-levels (3 km height). An important observational result of this study is that the most rapid rise rates of the towers coincide with or directly follow merger. This relationship is also evident in the modelling by Tao and Simpson, which shows low-level convergence between the approaching gust fronts assisting the development of cloud updraughts in the merger area.

Details on the merger process are difficult to define with the data available for this study. For the Melville Island system, C2 was first detected at 1439 CST within the loosely organised line L2 and it existed prior to any documented mergers. Cell C2 remained quasi-stationary throughout the merger process as the multicellular storm complex L1 approached from the north-east. Both L1 and L2 were aligned along the direction of the 700 mb to 950 mb shear, whereas the bridging between L1 and L2 was essentially along the direction of the 700 mb flow. Line L1 continued its southwestward movement around the southern side of C2. The northern end of L2 continued to move to the southwest and the southern edge dissipated. The result was the inverted V structure referred to earlier. The centre of the inverted V was dominated by C2, the east-southeast flank being the continuation of L1 and the western flank the continuation of L2.

In this case, the strongest growth of new cells was not seen over the bridging region, as is so common in Florida. In most (but not all) merging examples studied by Tao and Simpson (1989), the new cells initiated over the bridges grew to be the dominant features. Here, the pre-existing cell C2 grew to dominate the merged complex. However, relative motion between L1 and L2 did lead to a merged complex dominated by C2, which underwent its most rapid growth at the time of the merger. Hence, the merged complex involved interactions associated with pre-existing meso-scale components as well as those from gust-front outflows within the PBL.

Reorientation of the system from an essentially east-west to north-south aligned system occurred after the most significant merging phase between 1543 CST and 1700 CST (see Fig. 7). Most turning or re-orientation of the system occurred on the southern and eastern flanks. This is the location within the complex where the westward spreading gust fronts are dominant. Examination of the vertical cross sections in Figs. 13 and 15 shows that eastward extension of L1, L2 and L3, which essentially always moved southwestward, had highly-slanted front-to-rear updraughts with strong evidence for descending rear-to-front flow beneath the updraught. This structure was not evident in the quasi-stationary parts of the storm (e.g. the centre of C2). Cold-pool production transporting the mid-level easterly momentum to the surface is assumed to be responsible for the development of new cells by the forced ascent of unstable, high-θ_e air to the southwest of the old cells. Downdraughts stabilised the subcloud layer and suppressed convection to the east by the downward transport of midlevel, low-θ_e air to the surface, thereby contributing to the reorientation of the cloud system.

After the merger, the southern flank cold pools move out over the ocean into an unmodified environment and continue to form new cells. Cold pools generated by cells on the northern flank, where reorientation was less evident, are likely to have encountered a cooler, modified environment over the island less favourable for initiation of new convection. Hence, storm reorientation is a result of the continued (if not accelerated) southwestward motion of the southern oceanic side of the complex as the northern portion moved more slowly to the west.

6.2 Mesocirculations and Middle-Level Rear-to-Front Flow

The radar data indicate an essentially east-west aligned vortex pair of maximum intensity near 8 km elevation. The mean radial velocity in Fig. 14b is estimated to change by $12\,m\,s^{-1}$ over a radius of 5 km, implying a vertical velocity of $\zeta_z = 2.4 \times 10^{-3}\,s^{-1}$. If this vortex pair were generated by updraughts rising through a layer with vertical shear of the horizontal wind (e.g., Rotunno, 1981;

Klemp and Rotunno, 1983; Simpson et al., 1986), the main shear in the cloud layer would have to be north to south, which is only the case between the 3 and 4 km levels. Although the numerical simulation of this island thunderstorm undertaken by Golding (1993) showed evidence for mesoscale vortices of $\sim 10^{-3}\,s^{-1}$ in magnitude about some updraughts at the 8 km level, they were aligned north-south as would be expected from the classical tilting interaction with the environmental shear. In addition the simulated vortices were transient in nature and of smaller scale than those deduced from the radar.

The deduced vortex pair may merely result from the radar view of the interior, convective-scale circulations. As shown in Fig. 14, the front-to-rear radial flow associated with the vortex in the 8–10 km height range corresponds to the region of echo constriction near 8 km and a possible WER near 9 km height. These features are suggestive of a strong updraught at this location, which, from the Doppler radar, appears to be slanted approximately 45° from the horizontal along $x = 6$ km.

To the west, the mid-level rear-to-front flow may well represent a mid-level downdraught region of the type described by Knupp (1987) and Kingsmill and Wakimoto (1991). The asymmetry in the echo reflectivity structure from 6–12 km height in Fig. 13a shows intense echoes in the region of the inferred updraught and weaker downward-notching echoes to the west in the region of the rear-to-front flow. The weaker echoes suggest evaporation and sublimation of hydrometeors between $x = -10$ to $x = 0$ km. Fallout of hydrometeors from the anvil above (see Fig. 13) and wake entrainment are possible sources for initiating such a downdraught. In a storm relative sense, the shear is directed towards the updraught from 8–12 km height. The vortices could also be a result of complex interactions between lines L1 and L2 at 1525 CST when cell C2 was most intense (Figs. 8 and 13a).

6.3 Comparison with Tropical-Oceanic Convection

Previous studies have shown that convection is relatively weak over the tropical and subtropical oceans with updraught velocities rarely exceeding $10\,m\,s^{-1}$ (LeMone and Zipser, 1980; Zipser and LeMone, 1980; Jorgensen et al., 1985). Reflectivities in these systems rarely exceed 50 dBZ and are confined to below 3 km height, as well as typically decreasing in intensity with height above the freezing level (Szoke et al., 1986; Szoke and Zipser, 1986). These modest radar profiles have been hypothesised to be a result of draughts that are not strong enough to transport sufficient numbers of large raindrops above the freezing level, (Zipser and LeMone, 1980), and are thus likely not to support the development of hail (Szoke and Zipser, 1986).

Island thunderstorms are likely to be much more intense than their oceanic counterparts. For radar beamwidths in excess of 2 km, maximum reflectivities of 52.5 dBZ near the melting level (Fig. 13a) suggest the presence of large ice (possibly small hail), which is consistent with copious amounts of frozen drops simulated in the cloud model. Such a radar distribution was not observed in GATE, despite the higher spatial resolution of that dataset (Szoke et al., 1986; Szoke and Zipser, 1986), but is similar in intensity to the median profiles of New England hailstorms (Donaldson, 1961; see Fig. 13 in Szoke et al., 1986). These results are not surprising given the substantially higher CAPE of the early afternoon Hector environment ($2783\,J\,kg^{-1}$) compared to pre-convective GATE environments ($1000\,J\,kg^{-1}$; Barnes and Sieckman, 1984). Although the high ($>17\,g\,kg^{-1}$) water vapour contents in both environments promoted the initial development of precipitation by warm rain processes, precipitation loading is likely to have been greater in the 22 November 1988 Hector because the surface mixing ratios were $4\,g\,kg^{-1}$ higher in the 1330 CST Garden Point sounding than in the mean GATE environment. In addition, it is reasonable to presume that CCN concentrations over the island are roughly similar to those over the surrounding ocean, such that cloud droplets would be converted rapidly into rain in island thunderstorms as in convective clouds over the ocean.

7. Summary and Conclusions

The evolution of the three dimensional structure of a maritime continent thunderstorm over Bathurst and Melville Island, north of Darwin had been investigated. The islands are flat and develop a sea breeze circulation in response to the

solar heating cycle. Initially, the convective life cycle is characterised by shallow non-precipitating convection in an intermediate dynamic regime in which organisation is mainly random with some possibility of cloud street organization. The initial convection and the sea breeze circulations warm and moisten the sub-cloud layer over the island. Radar observations and modelling of the initial precipitating cells indicate that the first rainfall is generated by warm rain processes.

The first deep convection consists of lines of multicellular stroms with southwestward propagating cold pools that subsequently merge, resulting in rapid vertical development to 20 km height. As in the Florida cases studied by Simpson et al. (1980), mergers are initially concentrated in the low-level sea breeze convergence along an east-west line parallel to the long dimension of the islands. Subsequent mergers of the deep convection results in a complex mesoscale system with deep and extensive updraughts that maximise rainfall production. Later in the day, downdraughts develop on the flanks of the merged region by precipitation loading and evaporation. The result is deeper, stronger cold pools and reorientation of the complex away from the typically east-west sea breeze aligment to a vertical shear dominated north-south direction. Draught structure inferred from Doppler radar shows clear evidence of front-to-rear updraughts slanted over rear-to-front downdraughts and a forward propagating cold pool at this time. This mature stage complex exists as a squall line that propagates off the coast resulting in significant rainfall production over the surrounding ocean.

Data presented herein together confirm extremely large vertical motions (with an upper limit approaching $60\,m\,s^{-1}$) and suggest mesoscale vortices were present in the merged complex. It is postulated that a negative pressure perturbation is produced on the downshear side of the updraught leading to entrainment of dry and potentially cooler air into the storm, resulting in cooling from mixing, evaporation and sublimation of hydrometeors. This cooling drives a mid-level down-draught that does not reach the surface.

Although model simulations indicate that ice physics play a surprisingly minor role in the vertical development of the storms, sensitivity experiments suggest that updraught intensities would be about 25% lower without ice processes. There is also evidence for rapid glaciation of supercooled water near 8 km height. The release of this latent heat and the large lapse rates at upper levels contribute to the upward increase of updraughts to maxima at 15–16 km. Increased boundary-layer θ_e temperatures during the day in response to solar heating of the island surface was crucial in accounting for the intensity and depth of the simulated convection, and it is consistent with the observed diurnal variation of island convection.

The vertical structure of the island thunderstorm closely resembles that of continental thunderstorms rather than oceanic convection. The implication is that island thunderstorms provide a vertical heating profile of latent heat release for the maritime continent region that is different from a purely oceanic region. Questions on how important these diurnal thunderstorms are in terms of the total latent heat release within the region require further investigation. Rawinsonde based budget studies of the apparent heating and moistening from these thunderstorms are presently under investigation.

The convection over the Indonesian archipelago consists of transient, large-scale oceanic disturbances and these diurnal island thunderstorms. The two types of convection have very different time scales and profiles of apparent heating (Holland and Keenan, 1993). Because of their stronger updraughts, higher tops, and persistent appearance, these island-produced[11] clouds in the maritime continent probably play the major role in both troposphere/stratosphere interaction and cloud electrification in the region. They may also provide a significant fraction of the total rainfall and associated latent heat release in the "warm pool" region, a postulate requiring further study.

Acknowledgements

The assistance of all those involved in th ITEX program is acknowledged especially Prof. B. R. Morton from Monash University and Jim Arthur from the Northern Territory Regional Office of the Bureau of Meteorology. The experiment would not have been possible without the access and assistance provided by the Tiwi Land Council and the Conservation Commission of the Northern Territory.

[11] Another persistent day time island cumulonimbus (which also was seen under cirrus overcast) was observed during TOGA-COARE over the flat western portion of New Ireland in the Solomon Islands (Personal communication from Dr. Tom Ackerman).

References

Atlas, D., Srivastava, R. C., Sekhon, R. S., 1973: Doppler radar characteristics of precipitation at vertical incidence. *Rev. Geophys. Space Phys.*, **2**, 1–35.

Balaji, V., Clark, T. L., 1988: Scale selection in locally forced convective fields and the initiation of deep cumulus. *J. Atmos. Sci.*, **45**, 3188–3211.

Banta, R., Hanson, K. R., 1987: Sensitivity studies on the continentality of a numerically simulated cumulonimbus. *J. Climate Appl. Meteor.*, **26**, 275–286.

Barnes, G. M., Sieckman, K., 1984: The environment of fast- and slow-moving tropical mesoscale convective cloud lines. *Mon. Wea. Rev.*, **112**, 1782–1794.

Bluestein, H. B., Jain, M. H., 1985: Formation of mesoscale lines of precipitation: Severe squall lines in Oklahoma during the Spring. *J. Atmos. Sci.*, **42**, 1711–1732.

Bluestein, H. B., McCaul, E. W. Jr., Byrd, G. P., Woodall, G. P., 1988: Mobile sounding observations of a tornadic storm near the dryline: The Canadian, Texas storm of 7 May 1986. *Mon. Wea. Rev.*, **116**, 1790–1804.

Chisholm, A. J., 1973: Radar case studies and airflow-models. Part I, Alberta hailstorms. *Meteor. Monogr.*, **36**, 1–36.

Clark, T. L., 1973: Numerical modelling of the dynamics and microphysics of warm cumulus convection. *J. Atmos. Sci.*, **30**, 857–878.

Colby, F. P., Jr., 1983: Convective inhibition as a predictor of the outbreak in convection in AVE-SESAME II. Preprints, *13th Conf. on Severe Local Storms*, Tulsa, *Amer. Meteor. Soc.*, 324–327.

Cotton, W. R., Stephens, M. A., Nehkorn, T., Tripoli, G. J., 1982: The Colorado State University three-dimensional cloud/mesoscale model – 1982. Part II: An ice phase parameterization. *J. Rech. Atmos.*, **16**, 295–320.

Donaldson, R. J. Jr., 1961: Radar reflectivity profiles in thunderstorms. *J. Meteor.*, **18**, 292–305.

Ebert, E. E., Holland, G. J., 1992: Observations of record cloud-top temperatures in tropical cyclone Hilda (1990). *Mon. Wea. Rev.*, **120**, 2240–2251.

Ferrier, B. S., Houze, R. A. Jr., 1989: One dimensional time-dependent modelling of GATE cumulonimbus convection. *J. Atmos. Sci.*, **46**, 330–352.

Ferrier, B. S., 1993: A double-moment multiple-phase four-class bulk ice scheme. Part I: Description. *J. Atmos. Sci.* (in Press).

Fletcher, N. H., 1962: *The Physics of Rainclouds*. Cambridge: Cambridge University Press, 386 pp.

Golding, B. W., 1993: A numerical investigation of tropical island thunderstorms. *Mon. Wea. Rev.*, **121**, 1417–1433.

Hallett, J., Mossop, S. C., 1974: Production of secondary ice particles during the rime process. *Nature*, **249**, 26–28.

Hallett, J., Sax, R. I., Lamb, D., Ramachandra Murty, A. S., 1978: Aircraft measurements of ice in Florida cumuli. *Quart. J. Roy. Meteor. Soc.*, **104**, 631–651.

Hallett, J., Keenan, T. D., Williams, E., 1990: Penetrative velocities of high level tropical convective clouds. *Amer. Geophy. Union Fall Meeting*, December 3–7, San Fransisco, CA.

Holland, G. J., Keenan, T. D., 1993: Atmospheric response to island convection. *Quart. J. Roy. Meteor. Soc.* (Submitted).

Horel, J. D., Wallace, J. M., 1981: Planetary scale atmospheric phenomena associated with the southern oscillation. *Mon. Wea. Rev.*, **109**, 813–829.

Houze, R. A. Jr., Geotis, S. G., Marks, F. D., West, A. K., 1981: Winter Monsoon convection in the vicinity of North Borneo. Part I: Structure and time variation of the clouds and precipitation. *Mon. Wea. Rev.*, **108**, 1595–1614.

Illingworth, A. J., Goddard, J. W. F., Cherry, S. M., 1987: Polarization radar studies of precipitation development in convective storms. *Quart. J. Roy. Soc.*, **113**, 469–489.

Janowaik, J. E., Krueger, A. F., Arkin, P. F., 1985: Atlas of outgoing longwave radiation derived from NOAA satellite data. NOAA Atlas No. 6. U.S. Dept. of Commerce, Washington, D.C.

Jorgensen, D. P., Zipser, E. J., LeMone, M. A., 1985: Vertical motions in intense hurricanes. *J. Atmos. Sci.*, **42**, 839–856.

Keenan, T. D., Holland, G. J., Manton, M. J., Simpson, J., 1988: TRMM ground truth in a monsoon environment: Darwin, Australia. *Aust. Meteor. Mag.*, **36**, 81–90.

Keenan, T. D., Morton, B., Manton, M. J., Holland, G. J., 1989: The Island Thunderstorm Experiment(ITEX)-A study of tropical maritime continent thunderstorms. *Bull. Amer. Meteor. Soc.*, **70**, 152–159.

Keenan, T. D., Morton, B. R., Shu Xu, Zhang, Nyguen, K., 1990: A climatology of tropical island thunderstorms over Bathurst and Melville Islands near Darwin, Australia. *Quart. J. Roy. Meteor. Soc.*, **116**, 1153–1172.

Keenan, T. D., Potts, R., Wilson, J., 1991: The Darwin area forecasting experiment: Description and preliminary results. *Aust. Meteor. Mag.*, **39**, 211–222.

Keenan, T. D., Carbone, R. E., 1992: A preliminary morphology of precipitation systems in tropical northern Australia. *Quart. J. Roy. Meteor. Soc.*, **118**, 283–326.

Keller, V. W., Sax, R. J., 1981: Microphysical development of a pulsating cumulus tower: A case study. *Quart. J. Roy. Meteor. Soc.*, **107**, 679–697.

Kingsmill, D. E., Wakimoto, R. M., 1991: Kinematic, dynamic and thermodynamic analysis of a weakly sheared severe thunderstorm over northern Alabama. *Mon. Wea. Rev.*, **119**, 262–297.

Klemp, J. B., Rotunno, R., 1983: A study of a tornadic region within a supercell thunderstorm. *J. Atmos. Sci.*, **40**, 359–377.

Knupp, K. R., 1987: Downdrafts within high plains cumulonimbi. Part I: General kinematic structure. *J. Atmos. Sci.*, **44**, 987–1008.

Kogan, Y. L., 1991: The simulation of a convective cloud in a 3-D model with explicit microphysics. Part I: Model description and sensitivity experiments. *J. Atmos. Sci.*, **48**, 1160–1189.

Krishnamurti, T. N., Kanamitsu, M., Koss, W. J., Lee, J. D., 1973: Tropical east-west circulations during the northern winter. *J. Atmos. Sci.*, **30**, 780–787.

Kuettner, J. P., 1971: Cloud bands in the earth's atmosphere: Observations and theory. *Tellus*, **23**, 404–425.

Lau, K. M., Chang, C. P., Chan, P. H., 1983: Short-term planetary-scale interactions over the tropics and mid-latitudes. Part II: Winter-MONEX period. *Mon. Wea. Rev.*, **111**, 1372–1388.

LeMone, M. A., Zipser, E. J., 1980: Cumulonimbus vertical events in GATE. Part I: Diameter, Intensity and Mass Flux. *J. Atmos. Sci.*, **37**, 2444–2457.

Lin, Y.-L., Farley, R. D., Orville, H. D., 1983: Bulk pa-

rameterization of the snow field in a cloud model. *J. Climate. Appl. Meteor.*, **22**, 1065–1092.

Lord, S. J., Willoughby, H. E., Piotrowicz, J. H., 1984: Role of a parameterised ice-phase microphysics in an axi-symmetric nonhydrostatic tropical cyclone model. *J. Atmos. Sci.*, **41**, 2836–2848.

Malkus, J. S., 1954: Some results of a trade-cumulus cloud investigation. *J. Meteor.*, **11**, 220–237.

Malkus, J. S., 1955: The effects of a large island upon the trade-wind airstream. *Quart. J. Roy. Meteor. Soc.*, **81**, 538–550.

Malkus, J. S., 1960: Recent developments in studies of penetrative convection and its application to hurricane cumulonimbus towers. In: Anderson, C. E. (ed.) *Cumulus Dynamics*, pp. 65–84, New York: Pergamon Press.

Malkus, J. S., Scorer, R. S., 1955: The erosion of cumulus towers. *J. Meteor.*, **12**, 43–57.

Manton, M. J., Cotton, W. R., 1977: Formulation of approximate equations for modelling moist deep convection on the mesoscale. Atmos. Sci. Paper No. 266, 62 pp. [Available from Colorado State University, Dept. of Atmospheric Science, Ft. Collins, CO 80523].

Miller, L. J., Tuttle, J. D., Knight, C. K., 1988: Airflow and hail growth in a severe northern High Plains supercell. *J. Atmos. Sci.*, **45**, 736–762.

Mohr, C. G., Miller, J. J., Vaughan, R. L., 1981: An interactive software package for rectification of radar data to three-dimensional cartesian coordinates. Preprints, *20th Conf. on Radar Meteorology*, Boston, MA. Amer. Meteor. Soc., 690–695.

Moncrieff, M. W., Green, J. S. A., 1972: The propagation and transfer properties of steady convective overturning in shear. *Quart. J. Roy. Meteor. Soc.*, **102**, 373–394.

Mossop, S. C., 1985: Secondary ice particle production during rime growth: the effect of drop size distribution and rimer velocity. *Quart. J. Roy. Meteor. Soc.*, **102**, 45–57.

Nicholls, M. E., Pielke, R. A., Cotton, W. R., 1991: A two-dimensional numerical investigation of the interaction between sea breezes and deep convection over the Florida Peninsula. *Mon. Wea. Rev.*, **119**, 298–323.

Oye, R., Carbone, R. E., 1981: Interactive Doppler editing software. *20th Conf. Radar Meteorology*, Boston, MA. Amer. Meteor. Soc., 683–689.

Ramage, C. S., 1968: Role of a tropical "maritime continent" in the atmospheric circulation. *Mon. Wea. Rev.*, **96**, 365–370.

Rasmusson, E. M., Arkin, P. A., 1985: Interannual climate variability associated with the El Niño/Southern Oscillation. *Coupled Ocean-Atmosphere models*. Amsterdam: Elsevier Science Publishers B.V.

Riehl, H., 1979: *Climate and Weather in the Tropics*. London: Academic Press, 611 pp.

Rotunno, R., 1981: On the evolution of thunderstorm rotation. *Mon. Wea. Rev.*, **109**, 577–586.

Rotunno, R., Klemp, J. B., Weisman, M., 1988: A theory for strong long-lived squall lines. *J. Atmos. Sci.*, **45**, 463–485.

Rutledge, S. A., Hobbs, P. V., 1984: The mesoscale structure and organisation of clouds and precipitation in midlatitude cyclones. XII: A diagnostic modelling study of precipitation development in narrow cold-frontal rain bands. *J. Atmos. Sci.*, **41**, 2949–2972.

Rutledge, S. A., 1991: Middle latitude and tropical mesoscale convective systems. *Rev. Geophys.* [Suppl]. **29**, 88–97.

Rutledge, S. A., Williams, E., Keenan, T. D., 1992: Studies of dynamics and electrification of deep convection and mesoscale clusters near Darwin, Australia. *Bull. Amer. Meteor. Soc.*, **73**, 3–16.

Scorer, R. S., Ludlam, F. H., 1953: Bubble theory of convection. *Quart. J. Roy. Soc.*, **79**, 94–103.

Simpson, J. S., 1983: Cumulus clouds; Interactions between laboratory experiments and observations as foundations for models. In: Lilly, D. K., Gal-Chen, T. (eds.) *Mesoscale Meteorology-Theories Observations and Models*. Dordecht: Reidel Publishing Co., 399–412.

Simpson, J. S., van Helvoirt, G., 1980: GATE cloud-subcloud interactions examined using a three-dimensional cumulus model. *Contrib. Atmos. Phys.*, **53**, 106–134.

Simpson, J., Wescott, N. E., Clerman, R. J., Pielke. R. A., 1980: On Cumulus mergers. *Arch. Meteor. Geophys. Biokl.*, **A29**, 1–40.

Simpson, J. S., McCumber, M., 1982: Three-dimensional simulations of cumulus congestus clouds on GATE day 261. *J. Atmos. Sci.*, **39**, 126–145.

Simpson, J. S., Morton, B. R., McCumber, M., Penc, R., 1986: Observations and mechanisms of GATE waterspouts. *J. Atmos. Sci.*, **43**, 753–782.

Simpson, J., Keenan, T., Ferrier, B., Simpson, R. H., Holland, G., 1993: Cumulus mergers in the maritime continent. *Meteorol. Atmos. Phys.*, **51**, 73–99.

Skinner, T. L., 1990: A study of the sea-breeze over Melville and Bathurst Islands and its role in the development of island thunderstorms, Dissertation submitted in partial fulfilment of B.A. (Hon), Monash University, Clayton, Australia, 151 pp.

Soong, S.-T., 1974: Numerical simulation of warm rain development in an axisymmetric cloud model. *J. Atmos. Sci.*, **31**, 1262–1285.

Szoke, E. J., Zipser, E. J., Jorgensen, J. P., 1986: A radar study of convective cells in GATE. Part I: Vertical profiles statistics and comparison with hurricanes. *J. Atmos. Sci.*, **43**, 182–197.

Szoke, E. J., Zipser, E. J., 1986: A radar study of convective cells in GATE. Part II: Life cycles of convective cells. *J. Atmos. Sci.*, **43**, 199–218.

Tao, W.-K., Simpson, J., 1989: A further study of cumulus interactions and mergers: Three dimensional simulations with trajectory analyses. *J. Atmos. Sci.*, **46**, 2974–3004.

Tuttle, J. D., Bringi, V. N., Orville, H. D., Kopp, F. J., 1989: Multiparameter radar study of a microburst: Comparison with model results. *J. Atmos. Sci.*, **46**, 601–620.

Turpeinen, O., Yau, M. K., 1981: Comparison of results from a three-dimensional cloud model with statistics of radar echoes on day 261 of GATE. *Mon. Wea. Rev.*, **109**, 1495–1511.

Wakimoto, R. M., Bringi, V. N., 1988: Operational detection of microbursts associated with intense convection: The 20 July storm during the MIST project. *Mon. Wea. Rev.*, **116**, 1521–1539.

Weisman, M. L., Klemp, J. B., 1982: The dependence of numerically simulated convective storms on vertical wind shear and buoyancy. *Mon. Wea. Rev.*, **116**, 504–520.

Williams, M., Houze, J. R. Jr., 1987: Satellite-observed char-

acteristics to winter monsoon cloud clusters. *Mon. Wea. Rev.*, **115**, 505–519.

Woodward, B., 1959: The motion in and around isolated thermals. *Quart. J. Roy. Meteor. Soc.*, **95**, 144–151.

Zipser, E. J., LeMone, M. A., 1980: Cumulonimbus vertical velocity events in GATE: Part II: Synthesis and model core structure. *J. Atmos. Sci.*, **37**, 2458–2469.

Authors' addresses: T. D. Keenan, Bureau of Meteorology Research Centre, P.O. Box 1289KGPO, Melbourne 3001; Australia; B. Ferrier, U.S.R.A., NASA Goddard Space Flight Center, Greenbelt, MD, U.S.A.; J. Simpson, NASA Goddard Space Flight Center Greenbelt, MD, U.S.A.